Department of Physics and Astronomy

University of Heidelberg

Master thesis

in Physics

submitted by

Roxana-Adela Chira

born in Temeschburg (Romania)

2013

What is the most reliable tracer of core collapse in dense clusters?

This Master thesis has been carried out by

Roxana-Adela Chira

at the

Institute for Theoretical Astrophysics in Heidelberg

under the supervision of

Prof. Dr. Ralf Klessen

Dr. Rowan Smith

Fakultät für Physik und Astronomie

Ruprecht-Karls-Universität Heidelberg

Masterarbeit

Im Studiengang Physik

vorgelegt von

Roxana-Adela Chira

geboren in Temeschburg (Rumänien)

2013

Wie kann man Kollapsbewegungen in dichte Haufen zuverlässlich beobachten?

Die Masterarbeit wurde von

Roxana-Adela Chira

ausgeführt am

Institut für Theoretische Astrophysik in Heidelberg

unter der Betreuung von

Prof. Dr. Ralf Klessen

Dr. Rowan Smith

Abstract

Context. In the last years surveys and studies have emphasised the importance of filamentary networks within molecular clouds as sites of star formation. Since such environments are more complex than those of isolated cores, it is essential to understand how the observed line profiles from collapsing cores are affected by filaments.

Aims. Emission lines are modelled from collapsing cores embedded in filaments using radiative transfer calculations. Line profile asymmetries are studied and compared to those expected for isolated cores.

Methods. In three cores I model the (1-0), (2-1), (3-2), (4-3), and (5-4) transition lines of six molecular tracers. Three of them, HCN, HCO^+ and CS, are optically thick while the other three, N_2H^+, $H^{13}CO^+$ and ^{13}CO, are supposed to be optically thin.

Results. I found that less than 50% of simulated (1-0) line profiles show blue infall asymmetries. The numbers of blue asymmetric line profiles increases at higher transitions to about 90% in the (4-3) transitions. The origin of non-blue asymmetric line profile features was localised in the filaments around the embedded cores by using Optical Depth Surfaces.

Conclusions. Even in irregular, embedded cores infalling gas motions can be traced by blue asymmetric line profiles of optically thick lines. The best tracer of our sample is the (4-3) transition of HCN, but the (3-2) and (5-4) transitions of both HCN and HCO^+ are also good tracers.

Zusammenfassung

Kontext. In den letzten Jahren haben aktuelle Beobachtungen und Studien die Wichtigkeit von Filament-artigen Netzwerken in Molekülwolken als Brutstätten neuer Sterne betont. Da solche Umgebungen viel komplexer sind als die isolierter Kerne, ist es essentiell, zu verstehen, wie die beobachteten Linienprofilen von kollabierenden Kernen von den sie umgebenen Filamenten beeinflusst werden.

Mittel. Die Emissionslinien, die aus kollabierenden, in Filamenten eingebetteten Kernen ausgesendet werden, werden mittels Strahlungstransportberechnugen modelliert. Die Asymmetrien der Linienprofile werden untersucht und mit denen verglichen, die von isolierten Kernen erwartet werden.

Methoden. In drei Kernen modelliere ich die Spektrallinien der (1-0), (2-1), (3-2), (4-3) und (5-4) Übergänge von sechs Molekülen. Drei von ihnen, HCN, HCO^+ und CS, sind optisch dick, während von den anderen drei, N_2H^+, $H^{13}CO^+$ und ^{13}CO, angenommen wird, dass sie optisch dünn sind.

Ergebnisse. Ich fand heraus, dass weniger als 50% der simulierten Linienprofile des (1-0) Übergangs blaue Einfallsasymmetrien aufzeigen. Der Anteil an blau asymmetrischen Linienprofilen nimmt bei höheren Übergängen bis zu etwa 90% im (4-3) Übergang zu. Die Ursprünge nicht-blauer Merkmale in den Linienprofilen konnte mittels der Optische Tiefe-Oberflächen in den Filamenten um die eingebetteten Kerne lokalisiert werden.

Fazit. Auch in irregulären, eingebetteten Kernen können Einfallsbewegungen der Gase durch blau asymmetrische Linienprofile optisch dicker Indikatoren nachvollzogen werden. Der beste Indikator unserer Probe ist der (4-3) Übergang von HCN, jedoch erweisen sich auch die (3-2) und (5-4) Übergänge von HCN und HCO^+ als gute Indikatoren.

Contents

1 Introduction **1**

1.1 Sites of Star Formation 5

1.2 Previous Work and Source Selection 6

1.3 Radiative Transfer 10

1.3.1 Emission 10

1.3.2 Absorption 12

1.3.3 Asymmetric Line Profiles 14

1.4 Tracer Molecules 17

2 Methods **21**

2.1 `RADMC-3D` Set-Ups 21

2.2 Normalised Velocity Difference δv 23

2.3 Number Density – Velocity – Diagrams 24

2.4 Optical Depth Surfaces 26

3 Results **27**

3.1 Line Profiles 27

3.2 Normalised Velocity Difference δv 31

3.2.1 Dependency on the Reference Line 33

3.3 Origin of Emission Features 34

3.3.1 Number Density – Velocity – Diagrams 38

3.3.2 Optical Depth Surfaces 39

3.4 Observational Considerations 49

4 Summary & Conclusion **55**

Appendix **57**

List of Figures **61**

List of Tables **79**

1 Introduction

Star-forming regions, like the Carina Nebula shown in Fig. 1.1, have been studied for many decades both from an observational and a theoretical point-of-view. The first people who believed stars form out of self-gravitating matter were Kant (1692) and Laplace (1796). Since then astronomers have gained more insights into the formation of stars in our Milky Way Galaxy and in other galaxies. In particular, in the last century new techniques and methods in both observation and theory have enabled astronomers to study the environments of newly forming stars in more details. This has led to a great improvement in our knowledge about the circumstances under which stars form.

Nowadays we know that stars form in dense nebulae, known as molecular clouds, where diffuse interstellar medium condensates (Larson 2003). A pioneer in understanding the physical processes of star formation was Jeans (1902). He was one of the first to study molecular clouds from a physical point-of-view by considering density perturbations within an infinite uniform, isothermal medium. As a consequence he established criteria for self-gravitating gas to become unstable and collapse, namely the *Jeans length*, λ_J, defined as

Figure 1.1: Carina Nebula (Credit: NASA)

$$\lambda_J = \frac{c_s}{\sqrt{G\,\rho}} \simeq 0.4 \text{ pc} \left(\frac{c_s}{0.2 \text{ km s}^{-1}}\right) \left(\frac{n}{10^3 \text{ cm}^{-3}}\right)^{-\frac{1}{2}} \tag{1.1}$$

and the *Jeans mass*, M_J, given by

$$M_J = \frac{\pi}{6}\,\rho\,\lambda_J^3 = \frac{\pi}{6}\,\frac{c_s^3}{G^{\frac{3}{2}}\,\rho^{\frac{1}{2}}} \simeq 2 \text{ M}_\odot \left(\frac{c_s}{0.2 \text{ km s}^{-1}}\right)^3 \left(\frac{n}{10^3 \text{ cm}^{-3}}\right)^{-\frac{1}{2}} \tag{1.2}$$

where G is the gravitational constant.

Jeans investigated the equilibrium between gravity and thermal pressure of a homogeneous gas of mass density ρ, number density n and a sound speed c_s. He found that only spheres with diameters smaller than λ_J are stable, whereas spheres with diameters greater than λ_J are unstable and will gravitationally collapse. Analogously, one can state that a sphere with a fix radius $\frac{1}{2}\,\lambda_J$ will collapse if the enclosed mass becomes bigger than the corresponding Jeans mass M_J. Furthermore, since $M_J \propto \rho^{-n}$ ($n > 0$, exact value depends on the given equation of state of the gas) the Jeans mass becomes smaller with ongoing collapse. Smaller overdense regions form which collapse themselves. This fragmentation leads to the formation of stars in clusters. Although Jeans neglected processes like a finite reservoir of gas, rotation, magnetic fields, and turbulence, the Jeans criteria still give a good estimate of the stability of potential sites of future star formation.

Regions of future star formation need to be dense and clumpy for being able to gravitationally collapse. Such clumps, and on smaller scales cores, are observed within filamentary networks in molecular clouds (e.g., Bergin & Tafalla 2007; Williams et al. 2000; Arzoumanian et al. 2011). They form by the interaction of different forces like gravity, turbulence, magnetic fields and thermal pressure (see Sect. 1.1). Analogously to the Initial Mass Function (IMF) of stars the Core Mass Function (CMF) can be similarly defined. This counts the numbers of core with a mass m within a certain mass interval dm. Motte et al. (1998) have shown that the CMF of star-forming regions is similarly shaped to the IMF and can also be described by a power law (Kroupa 2002) or lognormal distribution (Chabrier 2002). This is very interesting since it suggests that there may be a direct connection between the formation of cores and the formation of stars (Motte et al. 1998; Padoan & Nordlund 2002) which is supported by the fact that stars form out of clusters of cores. Both gravitational fragmentation and turbulence lead naturally to power law distributions (Larson 1973; Elmegreen & Mathieu 1983; Padoan & Nordlund 2002). But there are many other effects which influence the evolution of a core into a star. For example, feedback produced by nearby stellar winds and outflows (Shu et al. 1988; Silk 1995; Myers 2008; Dale & Bonnell 2008), supporting magnetic fields (Heitsch et al. 2001; Tilley & Pudritz 2007) and competitive accretion (Zinnecker 1982; Bonnell et al. 1997, 2001) have an huge impact on the outcome of local star-forming processes which cannot be predicted from the very first core stage. Furthermore, theoretical studies have shown that the transformation of the CMF into the IMF is not that easy, but is affected by, e.g., an assumed constant efficiency and multiplicity (Alves et al. 2007; Goodwin et al. 2008; Smith et al. 2009a). Even the definition of what a core is and what its mass is depends on aspects like the choice of parameter (e.g. density, potential well), the resolution of the data, the local environments and the estimated dust temperatures.

When a core of gas in a molecular cloud becomes gravitationally unstable it collapses and the core centre becomes optically thick (Tohline 1982). Since the gas cannot be cooled efficiently, it is heated and the molecules within dissociate until the centre form a hydrostatic "Class 0" core which is called a protostar. In this phase the protostar accretes more material from its surrounding envelope. The luminosity of the protostar is now dominated by accretion. With time the material with higher angular momentum forms an accretion disk around the protostar, which will be the site of planet formation. In addition, a fraction of this material is launched into outflows and jets by the now "Class I" protostar. During this phase the envelope is cleared out until it is nearly gone in the "Class II" phase where accretion begins to come to a halt. Since the central temperature of the star is still not high enough to burn hydrogen the protostar starts contracting. In this process, which is called pre-main sequence or "Class III" phase, the potential energy of the (T Tauri) star is equally converted into thermal energy, which heats the centre, and luminosity. Meanwhile the disk thins out more until only a debris disk remains which may contain planets. At the time when the central temperature of the star reaches about 10^6 K hydrogen burning ignites and the star begins its main sequence. Fig. 1.2 sketches each evolutionary step and gives further information about bolometric temperatures, time-scales and masses.

Nevertheless, there are still many unanswered questions concerning the processes involved in star formation. In particular the formation of filamentary structures within molecular clouds and their contribution to, and influence on star-forming cores are not totally clear.

The question this thesis investigates is how and to which degree observations of molecular line profiles of cores are influenced by the surrounding filaments. The aim is to study the origins of line profile features and find a tracer which most reliably describes on gas motions within the core, without being perturbed by dense material in the envelope.

The thesis is outlined as follows: In the remaining part of Chapter 1 I will characterise molecular clouds and the environments of star-forming regions within them. I will introduce previous work on the underling simulations by Smith et al. (2009a,b, 2011, 2012) and the source selection criteria. There will be a short overview about the basic principals of the radiative transport methods I used and the line profile behaviours I want to investigate. Finally, the used tracers will be introduced.
In Chapter 2 I will introduce the technical tools and set-ups I use for my studies. The results are presented and discussed in Chapter 3. Chapter 4 provides a summary and the conclusion.

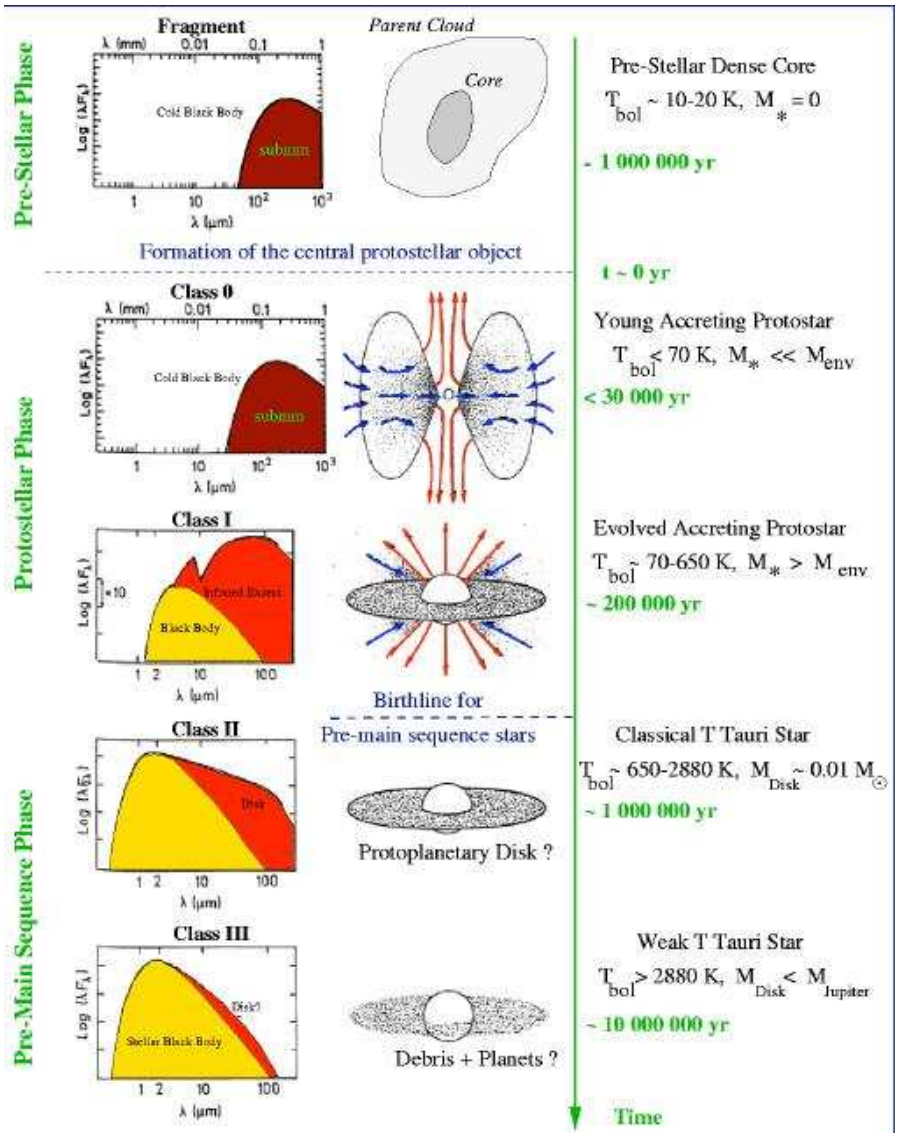

Figure 1.2: Empirical sequence for star formation and circumstellar evolution of a single star (André 2011) from a prestellar cloud core to a Class III young stellar object, based on the shape of spectral energy distribution (left), the bolometric temperature and mass of circumstellar (envelope & disk) material indicated on the right from Lada (1987); Andre et al. (1993); Myers et al. (1998)

1.1 Sites of Star Formation

As previously mentioned stars form along filaments in molecular clouds. Molecular clouds normally have sizes up to 15 pc, masses on the order of 10^3 - 10^4 $M_\odot$ and temperatures about 10 K (Bergin & Tafalla 2007, and Table 1.1). They are called molecular clouds, because they mainly consist of molecular hydrogen and other molecules, like CO. They can be observed as dark silhouette against the strong galactic background emission or as clouds lighted by nearby stars or stars which are still embedded (Simon et al. 2006; Peretto & Fuller 2009; Perault et al. 1996; Egan et al. 1998). Molecular clouds also consist of dust which makes the clouds opaque against visible light and light at higher frequencies. Although this makes it harder for observers to study the processes in the interior of a molecular clouds, it also prevents the molecules, which are the main coolants within the cloud from being destroyed by UV radiation and cosmic rays.

However, at longer wavelengths, particularly in the infrared and radio regimes, it is possible to look into the clouds and study their properties. This is mainly done by using emission and absorption lines of molecules. Since molecular hydrogen cannot be observed directly as it lacks a dipole moment, CO and its isotopes that trace diffuse gas are popular tracers in star-forming regions (e.g., Pineda et al. 2008). These species freeze out at densities higher then 4×10^4 g cm^{-3}. Therefore observations of nitrogen bearing molecules, like NH_3 and HCN, are in wide use.

The shapes of line profiles of molecular tracers mirror the conditions of the gas which can be extracted with the help of radiative transfer (see Sect. 1.3). In this way astronomers learn a lot about the properties of molecular clouds. A short summary is given in Table 1.1.

In the last years new observational techniques have permitted surveys of thermal dust emission, like ATLASGAL (Schuller et al. 2009), BOLOCAM (Aguirre et al. 2011), *Spitzer* (Werner et al. 2004) and *Herschel* (Pilbratt et al. 2010). They have emphasised that molecular clouds are not as homogeneous as Jeans assumed, but rather consist of substructures with clumps and cores (nomenclature adapted from Bergin & Tafalla 2007, see also Table 1.1) which are connected by filaments (Williams et al. 2000; Elmegreen 1993; Elmegreen et al. 2000; André et al. 2010; Arzoumanian et al. 2011; Peretto et al. 2012).

The formation of molecular clouds, their substructures and the condensation of gas into stars are results of the interactions between gravity which acts on wide ranges of scales, and a combination of forces which counter gravity on different scales (e.g., galactic tidal forces, turbulence, magnetic fields, thermal pressure, and centrifugal forces). On

	Clouds	Clump	Core
Mass ($M_\odot$)	10^3 – 10^4	50 – 500	0.5 – 5
Size (pc)	2 – 15	0.3 – 3	0.03 – 0.2
Mean Density (cm^{-3})	50 – 500	10^3 – 10^4	10^4 – 10^5
Velocity Extent (km s^{-1})	2 – 4	0.3 – 3	0.1 – 0.3
Gas Temperature (K)	≈ 10	10 – 20	8 – 12

Table 1.1: Properties of clouds, cores and cores (adapted from Bergin & Tafalla 2007).

scales of molecular clouds turbulence, magnetic fields and thermal pressure are the most important of those forces. The turbulence in molecular clouds is supersonic, but on scales of prestellar cores ($\sim$ 0.05 – 0.1 pc) it is subsonic. The shocks which are consequently produced compress the gas into filamentary or clumpy structures (Ostriker et al. 1999, 2001; Klessen et al. 2000; Mac Low 2003; Mac Low & Klessen 2004; Padoan et al. 2001) which collapse further into clusters of subsonic, star-forming cores (Arzoumanian et al. 2011; Inutsuka & Miyama 1997; Motte et al. 1998; Lada & Lada 2003). In particular massive stars (with masses greater than 8 $M_\odot$) seem to form in such clusters (Peretto et al. 2006; Bonnell et al. 1998; McKee & Tan 2003).

1.2 Previous Work and Source Selection

The work presented here is based on Giant Molecular Cloud (GMC) simulations first presented in Smith et al. (2009a). These use a three-dimensional (3D) smooth particle hydrodynamics (SPH, Monaghan 1992) code to investigate star-forming gas.

The GMC is set up as a cylinder with a height of 10 pc and a radius of 3 pc. It contains 10^4 $M_\odot$ in 5.5 $\times$ 10^6 particles which provides an average mass resolution of 0.18 M$\odot$ (Bate & Burkert 1997). The dynamical timescale is about 4.7 $\times$ 10^5 yrs and the simulations have been terminated after 1.4 $\times\, t_{dyn}$ ($\approx$ 6.6 $\times$ 10^5 yrs).

The code includes self-gravity and sink particles which represent the sites of star formation. The mass is not homogeneously distributed within the cylinder, but such that the density is high enough for the gas to be overbound at the one side, and low enough for the gas to be underbound at the other side. With this a density gradient, and thus a pressure gradient (see below), has been inserted in order to represent a range of star-forming environments.

For simulating heating and cooling a barotropic equation-of-state $P = k\,\rho^\gamma$ is intro-

duced with

$$\gamma = \begin{cases} 0.75 & \rho \leq \rho_1 & \text{line cooling} \\ 1.00 & \rho_1 \leq \rho \leq \rho_2 & \text{dust cooling} \\ 1.40 & \rho_2 \leq \rho \leq \rho_3 & \text{heating due to opt. thickness at IR} \\ 1.00 & \rho_3 \leq \rho & \text{allow sink particles} \end{cases} \tag{1.3}$$

where $\rho_1 = 5.5 \times 10^{-19}$ g cm^{-3}, $\rho_2 = 5.5 \times 10^{-15}$ g cm^{-3} and $\rho_3 = 2.0 \times 10^{-13}$ g cm^{-3} (Smith et al. 2009a, and references).

Furthermore, a Burger velocity field, following a Larson's $P(k) \sim k^{-4}$ power law, is inserted. In the beginning the amount of turbulence is normalised such that the initial total kinetic energy balances the initial total potential energy. The turbulence has not been driven artificially in the course of the simulation, but is maintained by gravitational collapse.

Over time the gas collapses and forms filaments with denser clumps and cores within. In this context, the definitions of Bergin & Tafalla (2007) are followed where 'clumps' are dense regions containing 50 – 500 $M_\odot$ within 0.3 – 3 pc and 'cores' even denser regions containing 0.5 – 5 $M_\odot$ within 0.03 – 0.2 pc. For identifying these potential wells have been used. A simplified sketch of the method in 1D is shown in Fig. 1.3. This method defines the clumps as either minimums in regions of positive potential or lowest contour which it shares with a neighbouring clump (Smith et al. 2009a). In Fig. 1.3 the feature on the right side would be identified as clump. Furthermore, they insert the parameter E_{rat} defined as

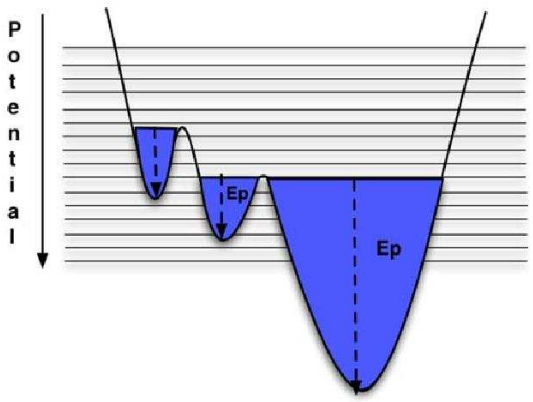

Figure 1.3: A 1D sketch of the potential well method for finding clumps (Smith et al. 2009a).

$$E_{rat} = \frac{E_p}{E_{therm} + E_{kin}} \tag{1.4}$$

where E_p represents the potential energy of the clump, E_{therm} its thermal energy and E_{kin} its kinetic energy. E_{rat} measures how bound a clump or core is. By definition, a clump or core is bound if its E_{rat} is bigger than 1, because gravity overbalances ther-

mal and kinetic energy from this point on. Smith et al. (2009a) find over 350 bound cores with an average mass of 0.7 $M_\odot$ within an effective radius (the radius of a sphere around the centre which contains about 68% of the clump's total mass) of about 0.012 pc (2400 AU) and velocity dispersions around 0.27 km s^{-1}. These properties correspond to those of "Class 0" star-forming cores.

While this potential well method works for simulated cores, it is not applicable to observational data, since it requires three-dimensional information of both positions and velocities of the cores to calculate the potentials. Thus, the results have to be converted into observable quantities, like column densities or line profiles of tracer molecules.

Another problem is that, although Smith et al. (2009a) have used quantities like the effective radius and tried to fit power laws to the density and temperature profiles of the bound cores assuming the cores to be spherical symmetric, the shapes of the majority of cores (about 75%) are only quasi-spherical. Most cores are embedded in filaments and elongated by them. They fragment into smaller substructures which are later identified as cores as well. Depending on the chosen boundaries, this causes differences between the centre of potential wells and centre of mass, and influences the outcomes when converting the data to observable quantities. The shapes of line profiles can change compared to profiles observed from spherical cores. Such changes lead to an underestimation othenf the number of cores undergoing dynamical collapse (Smith et al. 2011).

This is why Smith et al. (2012) select three of the non-spherical cores and investigate how reliably line profiles of molecules trace gas motions. The selected cores are already collapsing, are embedded in filaments, and will form sink particle in future. The latter biases the sample towards "real" star-forming regions and, since the cores are the smallest bound structures, helps to study the line profiles without worrying about the possibility that the cores may dissolve. The three cores of are labelled as Core A, B and C. The same nomenclature has been adopted here. Each of these three cores contains dense gas with number densities on the order 10^4 to 10^7 cm^{-3}, masses of 6.4 $M_\odot$, 12.3 $M_\odot$ and 14.7 $M_\odot$ and column densities on the order 10^{22} to 10^{23} cm^{-2}. All these properties are in good agreement with observed low-mass star-forming regions (Smith et al. 2012; Hacar & Tafalla 2011).

The work has been motivated by different studies of blue infall asymmetries in line profiles of optically thick species (Zhou et al. 1991; Zhou 1992; Walker et al. 1994; Myers et al. 1996). First calculations for blue asymmetries observed in collapsing cores were done by Zhou (1992). Although the observations of the Bok globule B335 by Zhou et al. (1993) confirmed the predictions, observations have shown that stars do not only form in isolated and spherical cores, but also in asymmetric cores which are embedded in

filaments and parts of multiple substructures (e.g., André et al. 2010). Line modelling has been extended to other, more realistic core symmetries, e.g. elongated cores (Walker et al. 1994) or cores formed within converging layers of gas (Myers et al. 1996). These studies, too, predict blue asymmetric spectra, as well as some observations have shown such. But in the majority of potential infall candidate cores blue asymmetric line profiles have not been observed (Gregersen et al. 1997; Gregersen & Evans 2000; Lee et al. 1999; Wu & Evans 2003; Fuller et al. 2005). Thus, more accurate modelling of both lines and chemistry, like freezing-out effects of carbon bearing species (e.g., CO, CS), in star-forming cores has become very important (Rawlings & Yates 2001; Tsamis et al. 2008; Stahler & Yen 2010; Tafalla et al. 2004).

For modelling the lines Smith et al. (2012) use the radiative transfer code `RADMC-3D`[6] (see Sect. 2.1 for more details). For this purpose the SPH data was mapped to 200^3 grids which correspond to a physical volume of 0.4^3 pc^3. The centres of the grid cubes correspond to the emission peaks of the cores. The cores and dense filaments were traced with the high density tracers HCN (1-0), CS (2-1) and N_2H^+ (1-0) (with critical densities on the order 10^5 – 10^6 cm^{-3}) at different sight-lines around the core centres.

Smith et al. (2012) find out that less than 50% of the modelled line profiles show the expected blue asymmetric shape (see Sect. 1.3.3 for more explanation). This is far too low, because a blue asymmetric line profile is an observable indicator for collapsing gas, and implies there is an underestimation of collapsing cores in observational surveys.

The aim of my project, is to continue the analysis of Smith et al. (2012) using more tracers and transitions for line modelling to find an optimal, reliable tracer for collapsing cores in dense clusters.

1.3 Radiative Transfer

The spectra of astronomical objects provide a lot of information about their properties, e.g. composition, temperature, abundances and gas motion. Thus, *radiative transfer* is a very important tool in astrophysics, because it describes the way information is transported via light. It describes the main cooling and heating processes and it is an important ingredient for driving chemistry and ionisation. Since my work is about optical depth effects on emission line profiles, I will concentrate on this aspect in this section. The following descriptions are adapted from the books by Tennyson (2005) and Böhm-Vitense (1989) and the lecture notes by Prof. Dr. Cornelis Dullemond[1] and Prof. Dr. Richard Pogge[2]. For further reading, please consult these works.

1.3.1 Emission

Astronomical spectra contain many different components. In star-forming regions emission lines of molecules are important, since they are efficient coolants. They also provide information about local temperatures, densities, abundances, masses and motions. These data are extracted by astrophysicists by knowing how atoms and molecules emit light. In this section we want to discuss different emission mechanisms of particles and assuming that the gas is optically thin (see Sect. 1.3.2).

In general, an atom or a molecule *emits* photons when it changes its quantum-mechanical state from a higher to a lower energy level. Famous examples in molecular clouds are the rotational lines of carbon monoxide (CO) and the inversion transitions of ammonia (NH_3). This emission may occur *spontaneously* or is *stimulated*. In both cases the energy of the emitted photon correspond to the difference of energy between the energy levels before (upper level, u) and after (lower level, l) emission:

$$\Delta E = E_u - E_l = h\,\nu \tag{1.5}$$

where E_i are the corresponding energy levels, h the Planck constant and ν the frequency of the emitted photon. In the case of stimulated emission the energy, direction and polarisation of the emitted photon is equal to the properties of the photon that stimulated the emission. If the gas is in local thermal equilibrium the population number density of

[1] Lecture Notes on "Radiative Transfer in Astrophysics" (`http://www.ita.uni-heidelberg.de/~dullemond/lectures/radtrans_2012/index.shtml`)
[2] Lecture Notes on "Physics of the Interstellar Medium" (`http://www.astronomy.ohio-state.edu/~pogge/Ast871/Notes/`)

energy levels are given by Boltzmann's law

$$\frac{n_u}{n_l} = \frac{g_u}{g_l} \exp\left(-\frac{E_u - E_l}{k_B T}\right) \tag{1.6}$$

where n_i presents the population number density of the energy level E_i, g_i its statistical weight, k_B the Boltzmann constant and T the temperature of the gas.

In dense regions, like molecular clouds, collisions between atoms and molecules are not negligible. Far from it, collisions are very important. For example, a high rate of collisions is necessary for a gas to become isothermal which is a commonly used assumption in star formation simulations. In molecular clouds collisions between molecular hydrogen and other molecules, like CO, is essential to cool the gas. Since H_2 lacks dipole moments which can be excited at common temperatures in such regions, it does not radiate effectively enough to cool on its own. Instead it passes parts of its energy to other molecules which become *collisionally excited* and emitted the energy later via radiation.

All three kinds of emission can be described by the Einstein coefficients A_{ul} (spontaneous emission), B_{ul} (stimulated emission and absorption) and C_{ul} (collisional emission). These coefficients give the rates at which each kind of emission occurs, and thus a measure of which process dominates. They depend on the properties of the molecule, the transition and the properties of the environment, which are represented by the temperature.

As the Einstein coefficients describe the emission processes mathematically, they can help to estimate when a transition line is *visible*. This is done by using the *critical density* which is given, assuming the gas to be in local thermal equilibrium and collisional excitation, by

$$n_{crit} = \frac{A_{ul}}{K_{ul}} \tag{1.7}$$

where K_{ul} is the collision rate coefficient, which is the product of typical collision cross section and average velocity of the particle. If the number density of the gas is smaller than the critical density, the population number of a higher energy level is smaller than predicted by the Boltzmann distribution. In this case the excitation temperature approximately equals the radiation temperature and the line is only poorly visible, if at all. But if the number density of the gas becomes higher than its critical density the gas thermalise and the population numbers are described by the Boltzmann distribution. Since different particles and transitions have different critical densities the strength of lines may give rough estimations of the densities in observed regions.

However, at lower frequencies (sub-millimetre and longer wavelengths) stimulated emission is more important than collisional emission. Thus, one has to take into account that the temperature $T_p = h\nu/k$ which correspond to the energy of the stimulating photons is in general far less than the kinetic temperature of the gas. A molecule which emits at in these frequency regimes needs higher densities than the critical density to thermalise. An example for this is the NH_3 $(J,K)=(1,1)$ inversion line at $\sim$ 23 GHz. Although its critical density is on the order of 10^3 cm^{-3}, the line does not become visible before the number density of the gas reaches 10^5 cm^{-3} (see Chapter V of Prof. Dr. Pogge's lecture notes[2]).

The different emission mechanisms do not only influence the population numbers of the energy levels of the atoms and molecules. They also affect the shape of the line profiles of the transitions. Normally, the line profiles of transitions are Lorentz shaped. Due to the Heisenberg uncertainty principle the lifetime of an energy state is finite and the oscillation becomes perturbed. As a consequence, the transition does not only happen at the quantum-mechanically clearly and uniquely defined central frequency ν_0, but also at a certain range of frequencies around ν_0. This range is called natural line width of a spectral line.

Since the atoms and molecules we observe in star-forming regions are neither at rest nor isolated the lines are broadened by different processes. As has been mentioned before, in dense environments collisions are important. They perturb the oscillations at random times. The line profiles become broader, but are still Lorentz shaped.

However, the velocity distribution of the gas, e.g. by thermal motion or microturbulence, causes that the emitted photons are Doppler shifted. This kind of broadening is called Doppler broadening and produce a Gaussian line profiles. When combining all these effects the resulting spectral line is represented by a Voigt profile, though the line profile becomes more Gaussian in turbulent regions, such as molecular clouds and star-forming cores.

1.3.2 Absorption

So far we have only talked about what happens when an excited particle emits photons and returns to its energetic ground-state. But we have not talked about how a particle is actually excited. This will be done now.

The ground-state of a particle is the one energy level with the lowest energy and therefore the stablest energy state. Thus, the particle needs to *absorb* energy, e.g. in form of photons or by collisions, to be able to excite any of its quantum-mechanical energy

states. Analogously to simulated emission, the absorbed photons need to have a certain amount of energy which is equal to the energy difference between the particle's energy state before and after absorption (see Equ. (1.5)). Due to these analogies, absorption, too, is mathematically described by the Einstein B_{lu} coefficients (instead of B_{ul} for stimulated emission).

The absorption line profiles of atoms, ions or molecules are similar to those of emission lines and are equally effected by broadening processes, but in an "inverse" fashion. Instead of an increase of intensity at a certain frequency, observers see a drop of intensity. The easiest case model is expressed by the Beer – Lambert law. It describes how the intensity of a light ray with an initial intensity $I_0(\nu)$ at a certain frequency ν is reduced when it travels through a homogeneous gas:

$$I(\nu, d) \;=\; I_0(\nu)\, e^{-\alpha_\nu d} \;=\; I_0(\nu)\, e^{-\sigma_\nu d\, n} \tag{1.8}$$

where α_ν is the extinction coefficient of the gas (which is just the inverse of the mean free path of a photon within this gas), σ_ν its absorption cross section, n its number density and d the distance which the light has already travelled through the gas.

The more general case, which also holds for non-homogeneous gases, is given by the radiation transfer equation:

$$\frac{dI_\nu}{ds}(s) \;=\; -\alpha_\nu\, (I_\nu(s) \;-\; S_\nu(s)) \tag{1.9}$$

$$\;=\; j_\nu(s) \;-\; \alpha_\nu\, I_\nu(s) \tag{1.10}$$

where s represents the position along the light of sight, S_ν the source function which corresponds to the emission function $j_\nu \;=\; S_\nu\, \alpha_\nu$. The source function of a blackbody emitter would be given by the Planck function. For the time being, we do not want to go into further details about the mathematical descriptions of radiative processes. For further reading see the lecture notes by Prof. Dr. Dullemond[1].

We now concentrate on how absorption effects line profiles. For this, we want to introduce the *optical depth*, τ, given by

$$\tau_\nu(s_0, s_1) \;=\; \int_{s_0}^{s_1} \alpha_\nu(s)\, ds \tag{1.11}$$

It measures how effective a gas (or a material in general) is able to absorb photons. Gases with a very low optical depth ($\tau \ll 1$) are called *optically thin*. In this case only a small fraction of the photons are absorbed in the gas. Thus, the observed amount of

absorption is directly proportional to the number of absorbers which is represented by the column density. But if the gas is *optically thick* ($\tau \gg 1$) this relation changes. The photons are absorbed and re-emitted several times while they travel through the gas. Hence, the number of observed absorptions is no longer directly proportional to the real number of absorbers. Of course, this also influences the shape of line profiles since the photons on the wings are less probably re-absorbed than those with frequencies closer to the central frequency ν_0 of the transition. Consequently, the lines are broadened and flatted (saturation) or reversed (self-absorption).

In the now following section we want to focus on the self-absorption features in line profiles of optically thick gas tracers and study how their shapes can be interpreted in context of gas motions in collapsing, star-forming cores.

1.3.3 Asymmetric Line Profiles

The shapes of line profiles are results of both emission and absorption processes along the line of sight. This has the advantage that one can learn a lot about the observed regions.

In star-forming regions the easiest case to consider is a spherical core as it is illustrated in the top panel of Fig. 1.4 (Smith et al. 2012; Evans 1999). The gas collapses radially onto the core. Since the observers see this from far-away outside the core, they only observe the velocity component along the line of sight. As shown in Fig. 1.4 the angle between the line of sight and the core centre increases the nearer the gas is to the centre. Assuming a $v_r \sim r^{-1}$ velocity distribution, the observed velocity components increase first until it reaches a maximal magnitude at some point before the core centre, and decrease afterwards again until it is zero at to the core centre (cf. Fig. 1.4, middle panel). If the density distribution also follows a r^{-n} power law (with $n > 0$) this produces a Gaussian line profile for optically thin species.

When observing an optically thick tracer, self-absorption has to be taken into account. Given a specific velocity the observer sees only the nearest point along the line of sight. Cf. Fig. 1.4, middle panel, the gas in regions marked with filled dots would be observed, but not the ones behind marked with the empty dots. A dip forms in the middle of the line profile (at $v_r \approx 0$), because of self-absorption from the surrounding envelope, and the line is no longer Gaussian. As is illustrated in the bottom panel of Fig. 1.4 the line profile now consists of two components. The blue and red dots correspond to those in the middle panel. The red part of the spectrum comes from the outer regions of the core which are nearest to the observer. Since the density is smaller in these regions the gas

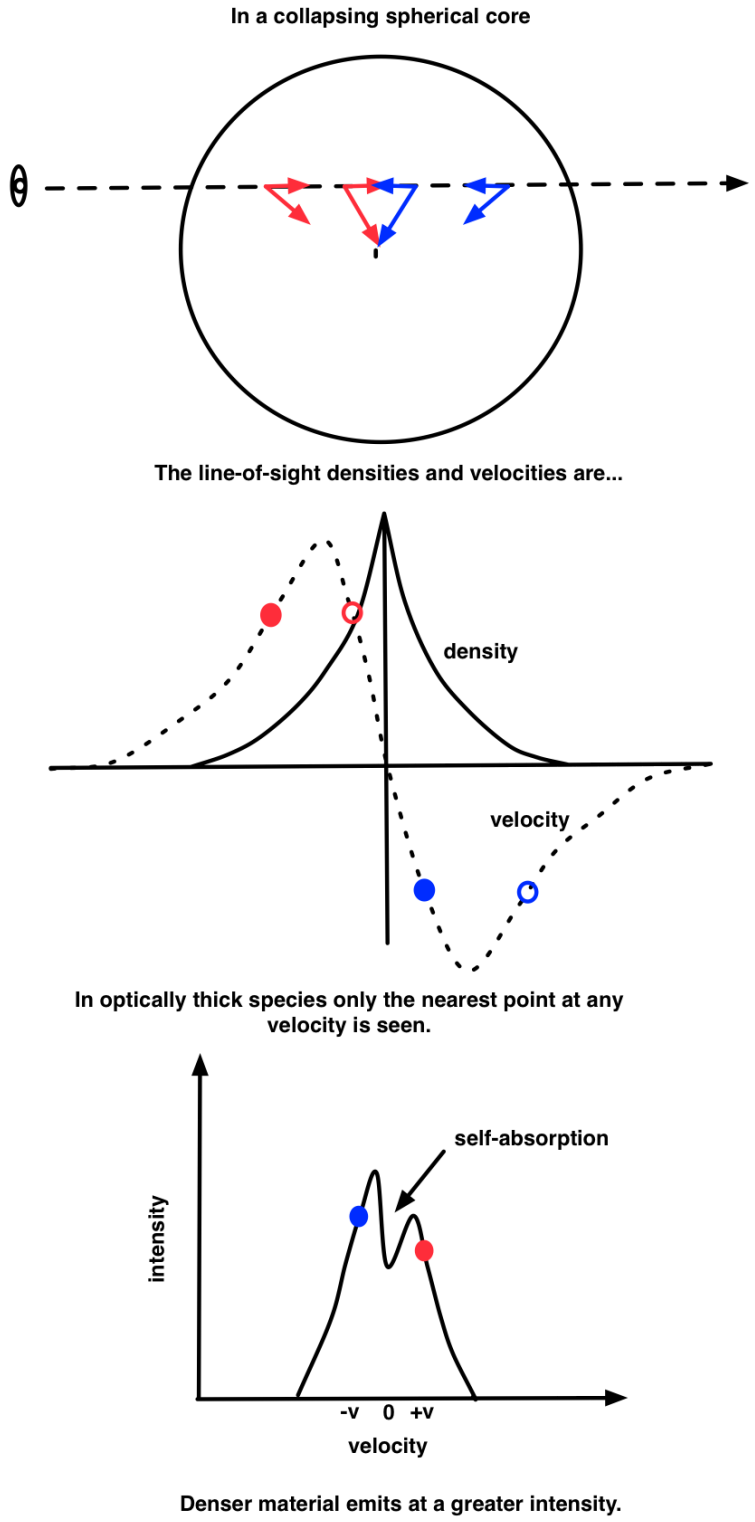

Figure 1.4: Sketch explaining the origin of blue asymmetric line profiles in collapsing, spherical cores (Smith et al. 2012).

here contributes little to the observed line profile. The gas corresponding to the blue part, on the contrary, is located in the inner regions just behind the core centre. Here the density is higher and more photons are emitted than in the red part.

Therefore, we expect the blue peak in the line profile to be higher than the red one, especially when we use a high density tracer (meaning a species with a high critical density) which emits from the dense central region. Such a line profile is called *blue asymmetric*. An example is given in Fig. 1.5 (left panel). On the contrary, if the core would expand or oscillate, the relation between the peaks would be the reverse and the observer would see a *red asymmetric* spectrum (cf. Fig. 1.5, right panel).

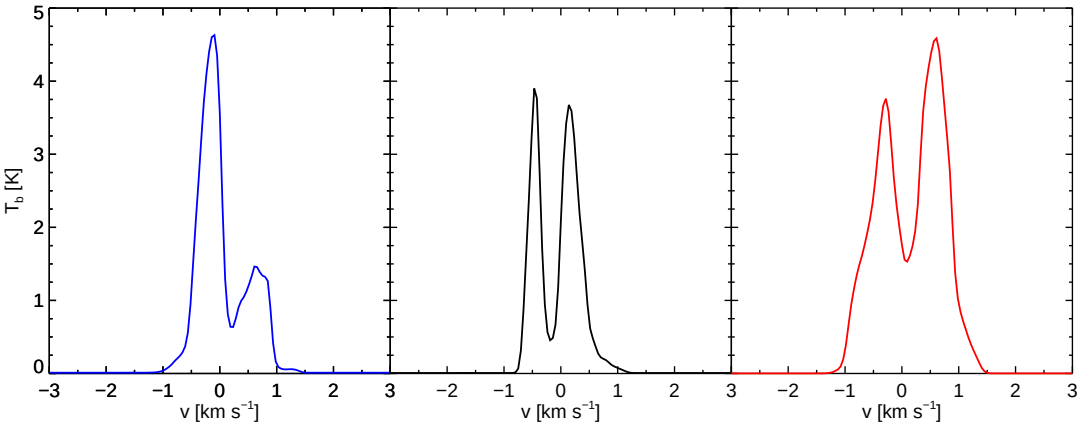

Figure 1.5: Examples for (*left*) blue asymmetric, (*middle*) ambiguous, and (*right*) red asymmetric line profiles.

As practical as this principle is for observations, one has to consider that it holds only for spherical cores. However, the majority of star-forming cores are not spherically symmetric (Smith et al. 2009a, , and Sect. 1.2). Smith et al. (2012) have already shown that less than 50% of line profiles of HCN (1-0) and CS (2-1) show a blue asymmetric shape although the cores have been collapsing. Many line profiles are *ambiguous*, meaning that either the difference between the peak heights are not significant or the line profiles are disturbed by other features (see Fig. 1.5, middle panel). There is also a fraction of line profiles that are red asymmetric. This is a great problem considering that the sample was biased to collapsing star-forming cores. It indicates that the simple case model introduced above may not always be applicable. The observations of cores in star-forming regions by Gregersen & Evans (2000), Lee & Myers (2011), Hartmann & Burkert (2007), and Sohn et al. (2007) have shown similar results. In all cases the fraction of observed blue asymmetric line profiles is less than 50%, as well as at least 30% of their

spectra are ambiguous. This implies that the number of observed star-forming cores is underestimated. Such an underestimation would also impact on other quantities like, for example, the core formation rate and star formation efficiency.

Consequently, it is very important to understand how asymmetric line profiles trace gas motions in dense clusters and which tracer is the most reliable. This will be investigated in this work by expanding upon the work of Smith et al. (2012). The following section will introduce the tracers we use and their properties and the next chapter the methods, before the results are presented in Chapter 3.

1.4 Tracer Molecules

The GMC simulations of Smith et al. (2009a) are in terms of gas density. We use abundance laws and model the lines of standard molecular tracers which can be detected using modern instruments.

The data of the tracers' quantum physical properties are taken from the Leiden Atomic and Molecular Database[3] (LAMDA, Schöier et al. 2005). LAMDA provides a collection of line data of different, astrophysically important atoms and molecules which are needed to calculate excitation levels in radiative transfer calculations. The files include information about energy levels, statistical weights, Einstein A-coefficients, collisional rate coefficients K_{ul}.

In total we use six tracers; three optically thin tracers, N_2H^+, ^{13}CO and $H^{13}CO$, and three optically thick tracers, HCN, HCO^+ and CS.

Diazenylium, N_2H^+, is one of the first ions which has been observed in the interstellar medium (Turner 1974). Since then it has been a very popular tracer for fractional ionisation, on-going chemistry, other molecules which are harder to detected (e.g., N_2 which lacks dipole moments), and density and velocity profiles of molecular clouds (Caselli et al. 2002), because it is supposed to hardly freeze out, even in dense cores. Bergin et al. (2002), however, have shown that this does not necessary need to be true and that variations are possible. For our calculations we used collision rates and Einstein coefficients by Daniel et al. (2005) and Schöier et al. (2005).

After molecular hydrogen, carbon monoxide, CO, and its isotopes, like ^{13}CO which we will use here, are the second most abundant molecules in the ISM. Since H_2 lacks dipole moments which are excited by common conditions in prestellar cores they are very important for astronomical studies. Thereby, each isotope traces different components of molecular clouds. Due to their low critical densities ($\sim 10^3$ cm^{-3}) they are common

[3] `http://home.strw.leidenuniv.nl/~moldata/`

markers for diffuse gas. The combination of low excitation conditions, high optical depth and freeze out behaviour (at $\sim 10^5$ cm^{-3}, Lee et al. 2004) makes CO to a good tracer for the outer envelopes of protostellar cores (Myers et al. 1996; Tafalla et al. 2002). Its isotope ^{13}CO is less abundant than ^{12}CO (by a factor of 1/77, Schöier et al. 2005), but still very common. Normally, it is supposed to be optically thin, but depending on the actual conditions within the observed regions it may become optically thick like CO (Carolan et al. 2008). Similar to CO, it freezes onto dust grains at higher densities. The collision rates and Einstein coefficients are taken from Schöier et al. (2005) and Yang et al. (2010) for our calculations.

The sulfur analogue of CO is carbon monosulfide, CS. Like CO it is optically thick, mainly traces diffuse gas in the envelopes of dense cores and is depleted forward the centres due to freezing onto dust grains (at about 2×10^4 cm^{-3}, Tafalla et al. 2002). Turner et al. (1992) calculated its collision rates and Einstein coefficients.

The third most abundant molecule in the ISM is the formyl ion HCO$^+$ and its isotopes (here only H^{13}CO$^+$). It has been observed by Buhl & Snyder (1970) for the first time. HCO$^+$ shows similar behaviours as HCN (see below) and is optically thick (Schenck et al. 2011), whereas its isotope H^{13}CO$^+$ is optically thin due to lower abundances. Flower (1999) and Schöier et al. (2005) provide the collision rates and Einstein coefficients.

In 1971 Snyder & Buhl also observed the optically thick dense gas tracer hydrogen cyanide, HCN, in the ISM. Its (1-0) transition is a triplet and each hyperfine line has a different optical thickness (in ascending order these are F(0-1), F(1-1) and F(2-1)). HCN has proved itself to be a good tracer for infall motions in prestellar cores (Sohn et al. 2007). Lee et al. (2004) found that the abundance of HCN is constant, although variations may be seen in the core centre. The collision rates and Einstein coefficients are supplied by Green & Thaddeus (1974) and Dumouchel et al. (2010).

We have modelled the (1-0), (2-1), (3-2), (4-3), and (5-4) transitions for all species. Table 1.2 summarises the transitions which we actually use for the discussion in Chapter 3. Table A.1 provides the rest frequencies and rest wavelengths of all transitions. It also lists the corresponding LTE critical densities.

In the case of N_2H^+ (1-0) transition we concentrate on the only single hyperfine component, 101-012, of the septuplet at 93.176 GHz since it is just needed as optically thin references line when calculating the normalised velocity difference (see Sect. 2.2). As well, we focus on the central hyperfine component of HCN (1-0) transition at 88.632 GHz.

Tracer	Transition Line	Critical Density n_{crit}	Optically
		cm^{-3}	
N_2H^+	J = (1-0)[2], (3-2)	1.6×10^5, 3.0×10^6	thin
^{13}CO	J = (3-2)	1.9×10^3	thin
$H^{13}CO^+$	J = (3-2)	1.7×10^5	thin
HCN	J = (1-0) – (5-4)[3]	1.0×10^6 – 9.7×10^8	thick
HCO^+	J = (1-0) – (5-4)[3]	1.6×10^5 – 1.7×10^7	thick
CS	J = (1-0) – (5-4)[3]	4.7×10^5 – 8.1×10^6	thick

[4] using only the isolated 101-012 hyperfine structure line
[5] meaning J = (1-0), (2-1), (3-2), (4-3), and (5-4)

Table 1.2: Properties of tracers. An overview. Given are the discussed transitions and the critical densities for LTE; the latter being estimated by $n_{crit} = A_{ul} / K_{ul}$ where A_{ul} represents the Einstein coefficient and K_{ul} the collisional rate coefficient at a temperature of 20 K.

Line profiles of each species and transition have been modelled at 256 evenly-spaced wavelengths around the corresponding rest wavelengths (which are put into the centre of the spectra).

The abundances of the species with respect to molecular hydrogen are given in Table 2.1 (as well as the corresponding references). In this study we assume constant abundances for all species. For the majority this is reasonable, but for ^{13}CO and CS. Their depletion laws have been neglected here for simplicity. Therefore, their abundances forward the core centres become artificially high and the results which have been obtained with them have to be threaten with caution (see Sect. 3.1).

2 Methods

2.1 RADMC-3D Set-Ups

For modelling radiative transfer I use the `RADMC-3D`[6] code. `RADMC-3D` accounts for scattering, thermal emission and absorption of both gas and dust. In this thesis we focus on modelling the line transfer in dense molecular gas.

Since I study dense clusters I use molecular tracers with high critical densities ($n_{crit} > 10^5$ cm^{-3}, cf. Table 1.2). The physical properties of the used species are offered by the LAMDA[3] (Schöier et al. 2005, see Sect. 1.4).

In this density regime one cannot assume *local thermal equilibrium* (LTE). Therefore, I use the *large velocity gradient* (LVG) approximation (Sobolev 1957; Shetty et al. 2011). LVG has the advantage that it calculates the photon escape probability by using the local velocity gradient.

A disadvantage of this approximation is that typical velocity differences are larger than the line widths, due to thermal line broadening and microturbulence. The Doppler shift between two neighbouring grid cells may become larger than typical line widths (cf. Fig. 2.1a). Thus, the shift is not resolved by `RADMC-3D` and the numerical integration may go wrong. One can avoid this problem by using the method of `Doppler Catching`[6] which has been discussed by Pontoppidan et al. (2009). This method provides an algorithm which localises such jumps and insert substeps to smooth the transition. This is illustrated in Fig. 2.1b. By doing this, the shift becomes resolvable for `RADMC-3D` which makes sure that the result of the numerical integration is right.

The gas temperature, number density of hydrogen and large-scale velocity distribution were taken from the GMC simulation. I assume a dust-to-gas ratio of 0.01 and a constant dust temperature of 20 K. Dust is needed, because we approximate the opacity by using thermal silicate grains. The level of microturbulence is set to 90 cm s^{-1}.

As said before, the number density of hydrogen was adapted from the GMC simulation and we assume molecular hydrogen to be the only collision partner for all tracers.

[6] The code is available with the permission of the main author, Cornelis Dullemond, at the webpage `http://www.ita.uni-heidelberg.de/~dullemond/software/radmc-3d/`. There is also a manual on the website including more detailed explanations of the different functions and parameters.

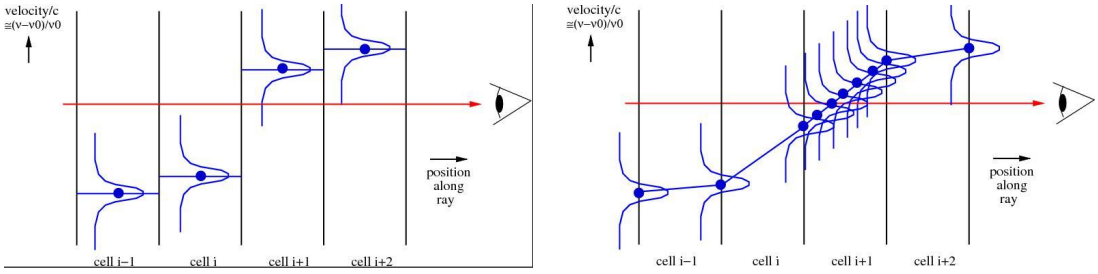

(a) without Doppler catching **(b)** with Doppler catching

Figure 2.1: Schematic illustration of `RADMC-3D` Doppler catching methods[4].

Furthermore, `RADMC-3D` needs the number densities of the studied species. To get them I assume constant abundances with respect to molecular hydrogen for each specie as listed in Table 2.1.

Tracer i	Abundance Law $[\chi_i = n_i/n_{H_2}]$	Reference
N_2H^+	1.0×10^{-10}	Aikawa et al. (2005)
^{13}CO	1.1×10^{-6}	Wu et al. (2012)
$H^{13}CO^+$	1.72×10^{-11}	Maruta et al. (2010)
HCN	3.0×10^{-9}	Lee et al. (2004)
CS	4.0×10^{-9}	Tafalla et al. (2002)
HCO^+	5.0×10^{-9}	Tafalla et al. (2002)

Table 2.1: Abundances of Molecular Tracers.

For deriving the spectra a Gaussian beam with a FWHM of 0.01 pc is used which corresponds to about 13.7 arcsec if the core is located at a distance of 150 pc (Smith et al. 2012).

We simulate line profile observations for each core, tracer molecule and transition in twelve different sight-angles. These are eight sight-angles with inclinations i between 0° and 315° in steps of 45° at constant rotation angle $\phi = 0°$ and four more with rotation angles ϕ between 45° and 180° in steps of 45° at constant inclination $i = 90°$.

2.2 Normalised Velocity Difference δv

Since we are interested in the formation and behaviour of asymmetries in line profiles, it is necessary to find a method with which spectra can be classified. One possibility is to look at each spectrum and decide individually whether it is blue or red asymmetric or ambiguous. But it is clear that this method is not efficient for a large sample and not necessarily reproducible in difficult cases.

A more quantitative method is needed. The normalised velocity difference δv (Mardones et al. 1997) is such a method. It is given by

$$\delta v \;=\; \frac{v_{thick} - v_{thin}}{\Delta v_{thin}} \tag{2.1}$$

where v_{thick} represents the central velocity of the higher peak in the spectrum of the optically thick species, v_{thin} the central velocity of the peak of the optically thin species (assuming the line profile has an Gaussian shape) and Δv_{thin} its velocity dispersion. The values are obtained by fitting a single Gaussian

$$G_s \;=\; T_{mb}\,\exp\left[-\frac{(v - v_{thin})}{2\,\Delta v_{thin}^2}\right] \tag{2.2}$$

to the optically thin line, where T_{mb} is the mean brightness temperature, and a double Gaussian

$$G_d \;=\; T_{mb,1}\,\exp\left[-\frac{(v - v_{thick,1})}{2\,\Delta v_{thick,1}^2}\right] + T_{mb,2}\,\exp\left[-\frac{(v - v_{thick,2})}{2\,\Delta v_{thick,2}^2}\right] \tag{2.3}$$

to the lines of the optically thick species, with $T_{mb,i}$ being the mean brightness temperatures of the ith line component. Hence,

$$v_{thick} = \begin{cases} v_{thick,1}, & \text{if } T_{mb,1} > T_{mb,2} \\ \delta v \;=\; 0, & \text{if } T_{mb,1} = T_{mb,2} \\ v_{thick,2}, & \text{if } T_{mb,1} < T_{mb,2} \end{cases} \tag{2.4}$$

In our simulation v_{thin} should be approximately 0 km s^{-1} and is theoretically not needed. But since the goal of this work is to understand observed line profiles, we have to take the data into account that is available to an observer doing these calculations. Effects like local standard of rest velocities etc. have to be considered. So, I kept v_{thin} as the reference point and calibrator.

The higher peak central velocity of the optically thick species, v_{thick}, in contrast, should differ from 0 km s^{-1}, either to positive or negative values depending on the symmetry of the spectrum. If the line profile has a red asymmetry the red peak, with positive central velocity (cf. Fig. 1.4), is higher. Thus, v_{thick} and δv are positive. On the other hand v_{thick} and δv become negative if the line profile is blue asymmetric if the blue peak is higher.

The disadvantage of this method is that spectra with ambiguous symmetries, meaning line profiles which cannot be identified as blue or red asymmetric clearly (e.g. because the peaks are nearly equally high), are hard to identify, because even the smallest difference between the brightness temperatures is detected. To identify such cases I introduce two criteria, namely

1. $\frac{|T_{mb,1}-T_{mb,2}|}{\max\{T_{mb,1},T_{mb,2}\}} < 10\%$ 2. $|v_{thick,1} - v_{thick,2}| < \Delta v_{thin}$

If one criterion is fulfilled (or both), δv is set to 0 km s^{-1} and the spectrum is classified as ambiguous.

2.3 Number Density – Velocity – Diagrams

As previously described the cores were chosen because they were not spherically symmetric, but irregular and embedded in filaments. Thus, their number density, n, and velocity, v, distributions differ significantly from the ideal case model presented in Fig. 1.4 and Sect. 1.3.3. Of course, this leads to changes in the line profiles compared to the theoretical model.

Before we investigate how line profile shapes are influenced, we need to know how gas and velocity are distributed in the cores. This is done with a number density – velocity – diagram (n - v - diagram). An example is shown in Fig. 2.2.

The n - v - diagrams consist of two plots. The bottom panel plots the number density against the line of sight radius z along which an observer looks at the core. In doing so the core centre is at $z = 0$ and the observer at $z = -\infty$. Thus, gas at a negative z is, from the observer's point of view, in front of the core, and gas with positive z behind it. x and y correspond to the perpendicular coordinates which would be mapped by the observer (cf. Sect. 2.4). The top plot shows the gas velocity distribution along z. In both plots the distributions within the line of sight are drawn with dashed line. Regions with number densities higher than 3×10^4 cm^{-3} are marked with solid black lines. The red coloured regions show the dense gas within the central core regions,

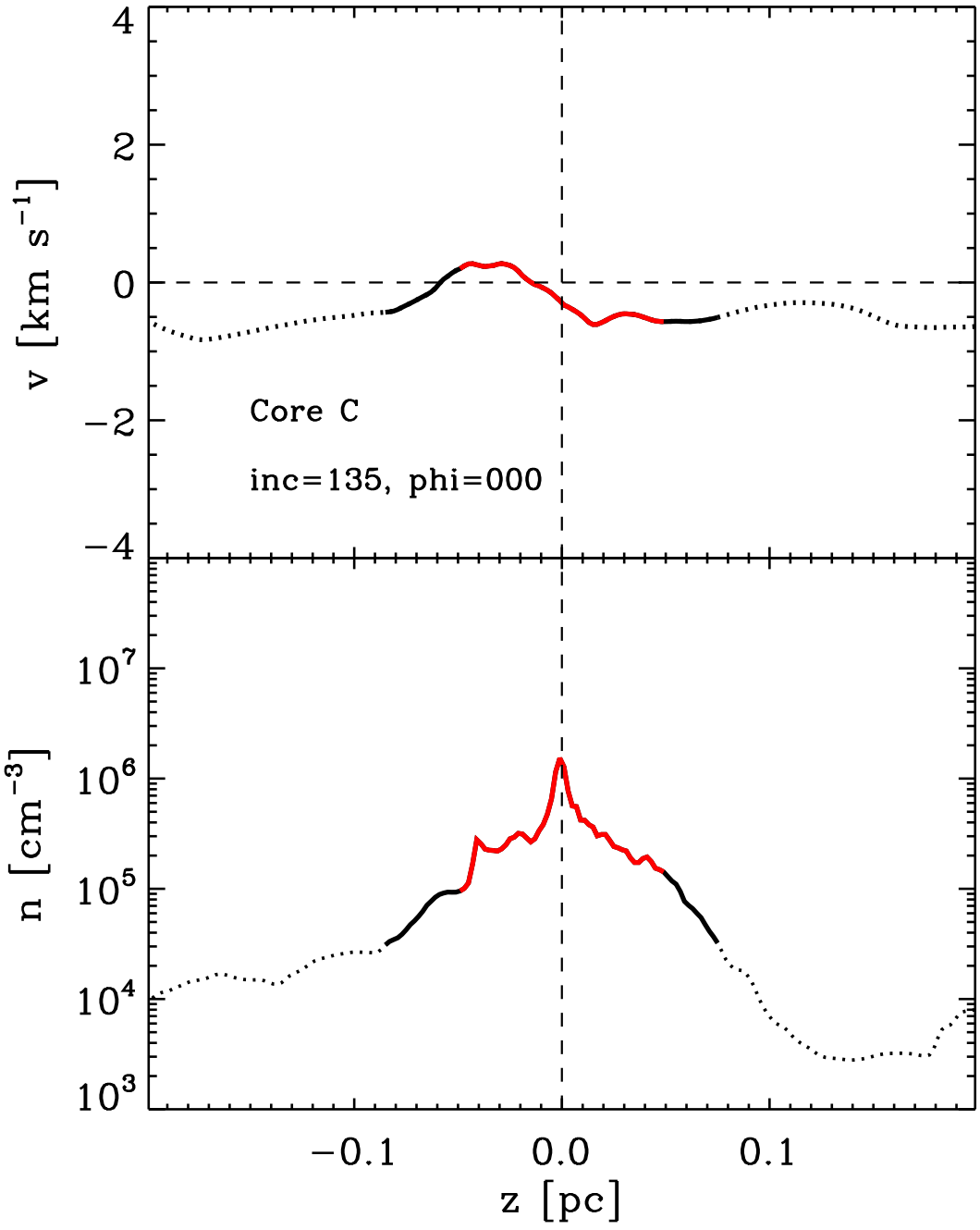

Figure 2.2: n - v - diagram of Core C at i =135° and ϕ =0°. The number density and velocity distribution are plotted with dashed lines. Thick black lines mark regions with number densities higher than 3×10^4 cm^{-3}, red lines such within a radius of 0.05 pc around the core centre.

approximated here as the volume within a radius of 0.05 pc around the core centre ($\sqrt{x^2 + y^2 + z^2} \leq 0.05$ pc).

So, how do these diagrams help? When the number density of the gas becomes higher than the critical density of the tracer, collisional excitation is significant and collisional de-excitation is faster than radiative de-excitation (Tennyson 2005). The emission is now dominated by collisions with the collision partner (in our case only H_2). The positions of peaks in the observed line profiles correspond to peaks in the number density distribution at the corresponding velocity. Using the n - v - diagrams it is possible to connect number density, z position and velocity with each other. Thus, we can reconstruct where emission features exactly come from or, the other way around, where we can expect features to be located in the spectrum. This helps to trace the origin of features which influence the asymmetry of line profiles.

2.4 Optical Depth Surfaces

Another way to locate the origin of emission features, especially for the optically thick tracers, is to look where each tracer actually becomes optically thick. For this I use the `tausurf`[6] function of `RADMC-3D`. The function returns the position where the optical depth, τ, of the gas reaches a certain value for the first time along z at a given wavelength. Here I look at the $\tau = 1$ surfaces at the rest wavelengths of each transition.

Fig. 3.5 shows an example. The *Optical Depth Surfaces* include two sets of information. The grey-scale background shows the emission of the tracer gas in logarithmic scales. It acts as a reference for the general structure of the core and surrounding filament as it would be seen by the observer. The green star in the middle indicates the location of the core centre. The coloured points in the foreground display the results of `tausurf`, thus the position where the tracer becomes optically thick. The colour of the dots refer to the corresponding line of sight radius z. Red colours symbolise positions in front of the core (along the line of sight) and blue colours positions behind the core. Thus, the redder the colour of a dot, the closer the surface is to the observer.

While the n - v - diagrams describe the distributions of number density and velocity in every detail, but they need all three-dimensional information about velocity and density. These are not available to observer. The advantage of the Optical Depth Surfaces is that they show which part of the total emitted light is actually observed by the observer. With this information it is possible to set limits to the "interesting" regions and to explain why features do not appear in the line profile although they have been predicted by the n - v - diagrams.

3 Results

Smith et al. (2012) have already found that observed asymmetries in line profiles of HCN and CS depend strongly on the sight-lines at which the observer looks at the core due to the structure of the filaments surrounding the core. This thesis continues the analysis by using more tracer species and transitions. It also investigates the origin of non-blue asymmetric line profiles and which transitions are most reliable for tracing gas motions in star-forming cores. In this chapter I will present the results.

First I will discuss the line profiles and their general behaviour, which will be studied more quantitatively when the classification based on the normalised velocity difference δv is introduced. Afterwards I will discuss the origins of emission features in more detail by looking closer at the density, velocity and optical depth distributions. In the end I will investigate the influence of noise on the results of line profile asymmetry classification.

3.1 Line Profiles

Optically Thick Tracers

As previously stated, a beam with a FWHM of 0.01 pc going directly through the core centre was used for calculating the line profiles. Fig. 3.1 shows the line profiles of the (1-0) transition of all species and cores seen at inclination and rotation angles of 0°. The line profiles of HCN, HCO^+ and CS show optical depth effects, such as the dip due to self-absorption (cf. Fig. 1.4).

However, contrary to the theoretical model presented in Sect. 1.3.3, many spectra are not blue, but red asymmetric or ambiguous. The line profile asymmetries at given inclination and rotation angles are not invariant like one would be inclined to believe.

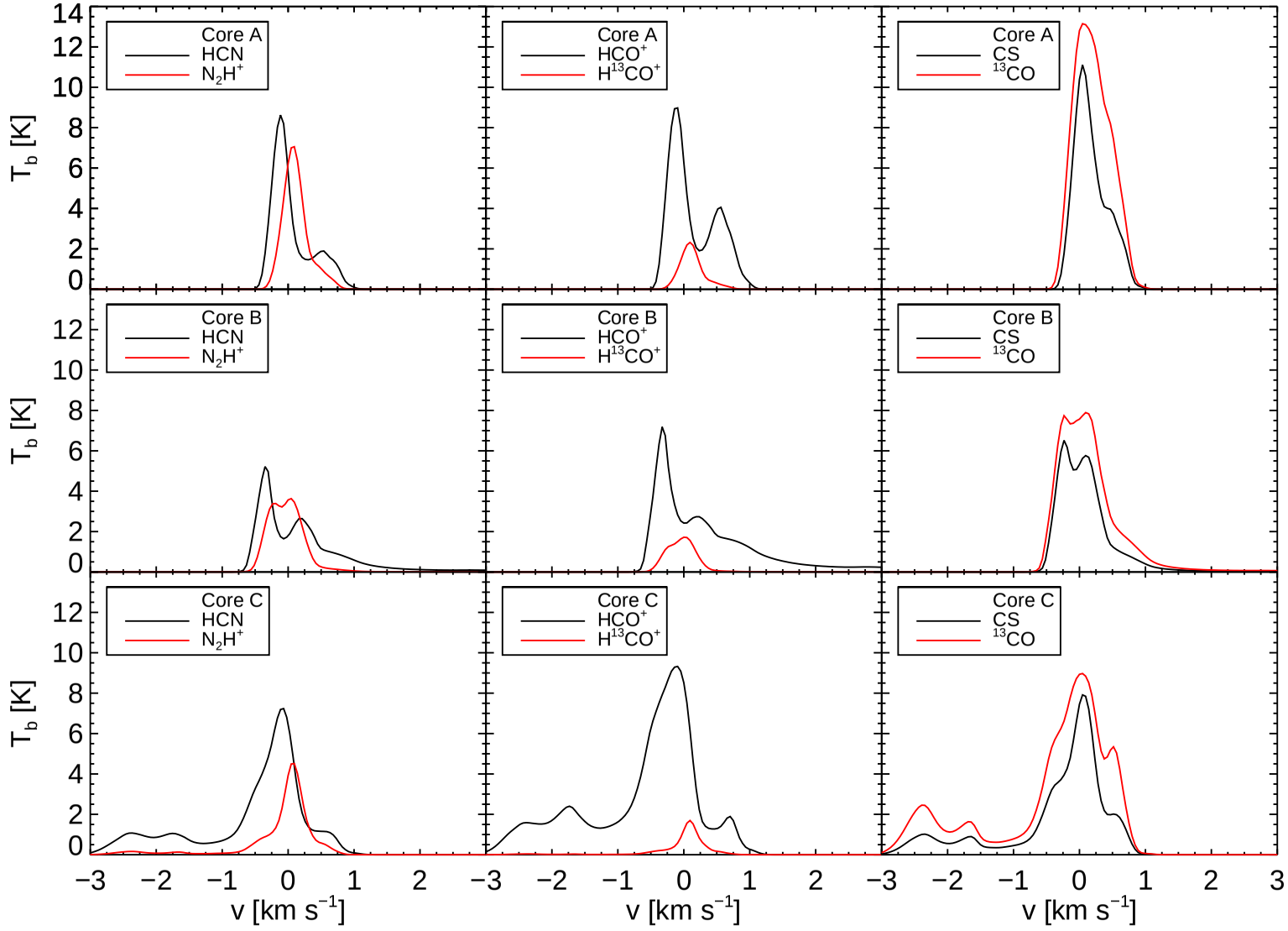

Figure 3.1: (1-0) transition lines of all tracer species in all cores at $i = 0^\circ$ and $\phi = 0^\circ$.

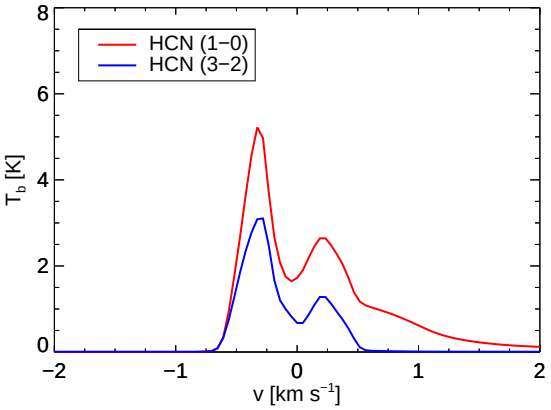

(a) Line profiles in Core A at $i = 180°$ and $\phi = 0°$. Both lines show blue asymmetry.

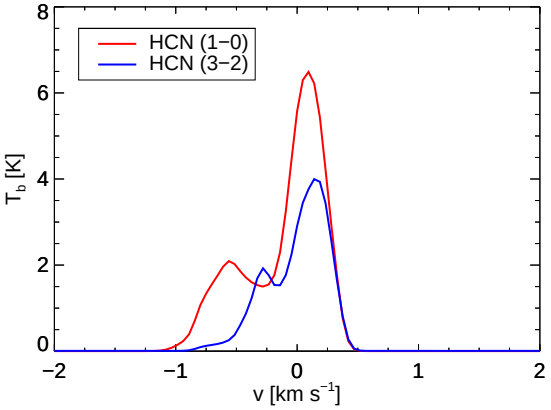

(b) Line profiles in Core B at $i = 90°$ and $\phi = 135°$. Both lines show red asymmetry.

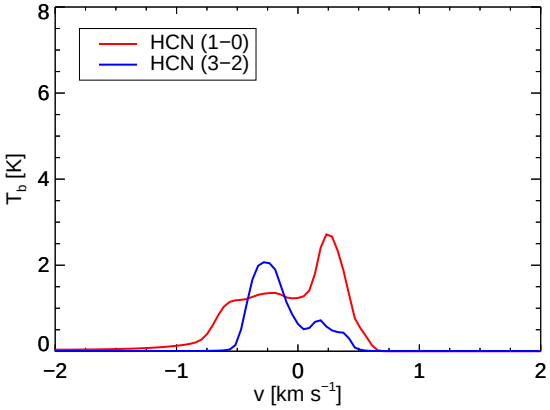

(c) Line profiles in Core B at $i = 0°$ and $\phi = 0°$. Both lines show different asymmetries. The line profile of HCN (1-0) is red asymmetric and the line profile of HCN (3-2) is blue asymmetric.

Figure 3.2: Exemplary line profiles of HCN (1-0) and (3-2) observed in our models. The three pictures show different cases where (a) both line profiles are blue asymmetric, (b) both are red asymmetric, or (c) both lines show different asymmetries.

Fig. 3.2 gives examples of HCN (1-0) and (3-2) line profiles for the most commonly occurring cases, namely that

- Fig. 3.2a : both lines are blue asymmetric which is the ideal case,
- Fig. 3.2b : both lines are red asymmetric which is the worst case, and
- Fig. 3.2c : the line profile of HCN (1-0) is red asymmetric, but the one of HCN (3-2) blue asymmetric which is the common case.

It has to be emphasised that, although only examples of HCN are given, HCO^+ and CS behave similarly. In particular the latter case is a very interesting result, because it shows that the red asymmetries in the line profiles are indeed real, but do not trace gas motions in the core. Consequently conclusions according collapse motions within the core region may turn out to be wrong when assuming the simple case model.

Optically Thin Tracers

The line profiles of N_2H^+ and $H^{13}CO^+$ look mostly Gaussian, as is expected for optically thin species. Unfortunately, there are also some line profiles of N_2H^+ and $H^{13}CO^+$, as well as the majority of line profiles of ^{13}CO that show optical depth features. In Fig. 3.1 this is the case in all line profiles observed in Core B. This behaviour indicates that these species, too, become optically thick.

This is a real problem, because N_2H^+, ^{13}CO and $H^{13}CO^+$ are required to be optically thin for our analysis, because they are used as reference lines in the δv calculations. Optical depth features in these line profiles worsen the Gaussian fit procedure and the obtained parameters. If the central velocity cannot be reliably calculated, this has a significant influence on the results of δv.

At this point we have to emphasise that we neglected the fact that carbon bearing species freeze out onto dust grains that high densities. In our study this would have been meaningful for CS and ^{13}CO (e.g. Tafalla et al. 2002). Since we have ignored this effect, the abundance of CS and ^{13}CO are artificially higher and the gases themselves optically thicker than it would have been observed. Especially in the core regions their densities should drop and this would have a significant impact up on the line profiles. Because the densities further outside would be higher than in the actual core region, the line profiles would be more affected by the filaments (see Sect. 3.3) and the line profiles would show more disturbing features compared to the expectation (which is a blue asymmetric line

profile in the case of CS and an optically thin spectral line in case of ^{13}CO). Thus, we ask the reader to treat the results derived with these tracers with caution.

Many line profiles, of both optically thick and optically thin tracers, have additional emission features which cannot be explained solely by the the influence of optical thickness. One example is given in Fig. 3.1. The lines observed in Core C consist of two components. There is a bright component around 0 km s^{-1} which belongs to the central regions we want to study. The second component at about -2 km s^{-1} is weaker and, according to the corresponding n - v - diagram, come from a dense region behind the centre. Fig. 3.3 shows the line profile of HCN (1-0) and the corresponding n - v - diagram for better comparison. The origin of these features will be discussed in Sect. 3.3 more explicitly.

3.2 Normalised Velocity Difference δv

In this section we quantify the characterisation of the line profiles. For this purpose we have already introduced the normalised velocity difference δv in Sect. 2.2. Shortly summarised one calculates the difference between the central velocities of the optically thin reference line and the highest line component of the optically thick tracer. The difference is then normalised by the FWHM of the optically thin line to reduce the bias due to different line widths (Mardones et al. 1997). Following the definition given in Eq. (2.1) a negative δv represents a blue asymmetric line profile, and a positive δv a red asymmetric line profile. We introduce two criteria for ambiguous line profiles: first that the relative brightness temperature difference of the peaks in the line profile of the optically thick tracer is smaller than 10%, and second that the absolute velocity difference is smaller than the FWHM of the reference line. The first criterion represents line profiles where either an observer could not classify the line clearly, or where observational difficulties, like noise, might cause problems (see Sect. 3.4). If either criterion are fulfilled the line profile is classified as ambiguous and its δv is set to 0 km s^{-1}.

Following Smith et al. (2012) we start our analysis by using N_2H^+ (1-0) as reference lines. The results are given in Table 3.1 and plotted Fig. 3.4a. Table 3.1 lists the mean and median δv as well as the fraction of line profiles in our sample classified as blue, red asymmetric or ambiguous for each transition of each optically thick species. Fig. 3.4a summarises the results. The figure shows the fraction of blue, red asymmetric and ambiguous line profiles at the individual transition. The numbers are summed up for all optically thick tracers. In both, table and figure, we see that for the (1-0) transitions

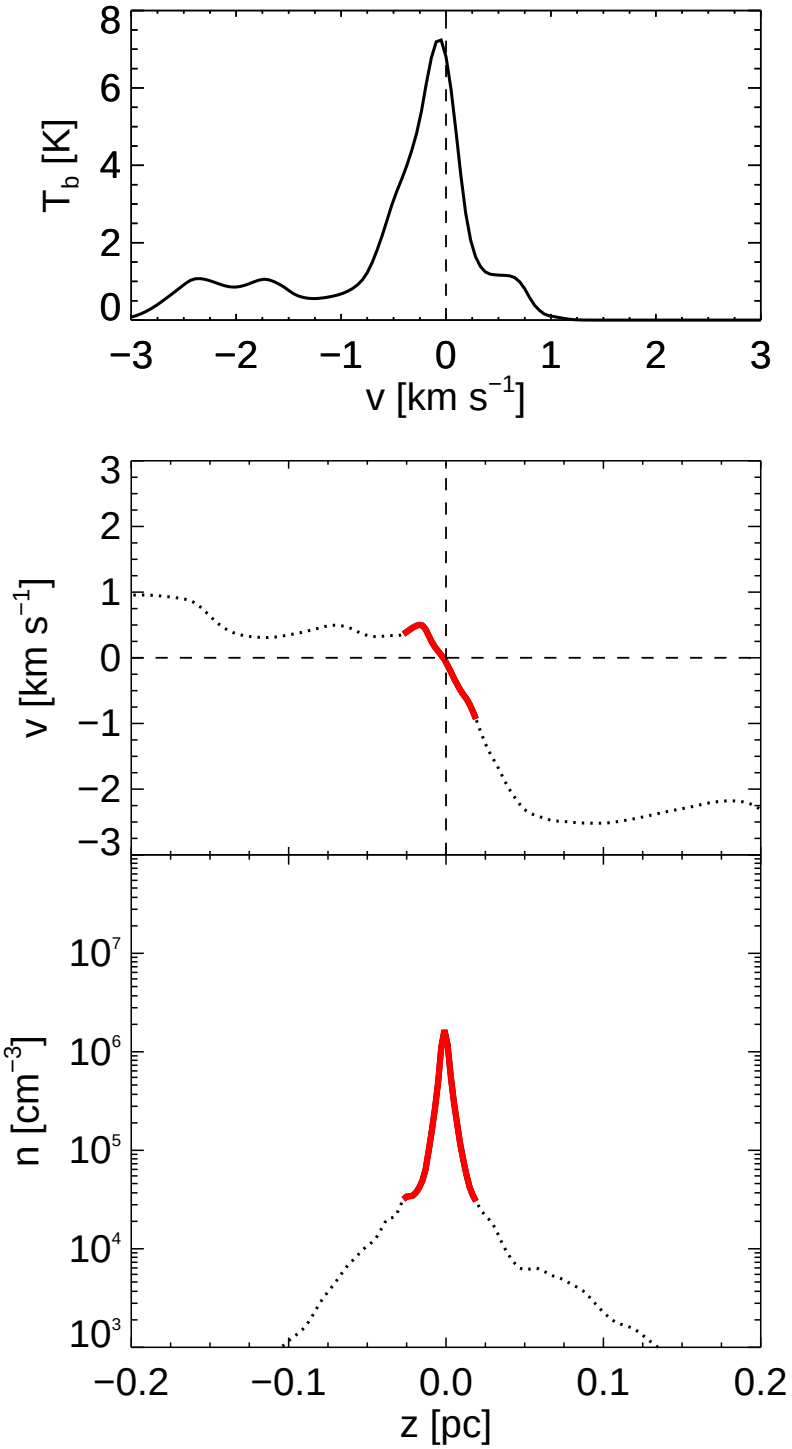

Figure 3.3: *upper panel:* Line profile of HCN (1-0) observed in Core C at $i = 0°$ and $\phi = 0°$. *lower panel:* n - v - Diagram of Core C at $i = 0°$ and $\phi = 0°$. The number density and velocity distribution are plotted with dashed lines. Thick black lines mark regions with number densities higher than 3×10^4 cm^{-3}, red lines mark areas within a radius of 0.05 pc around the core centre. One sees that the origin of the line profile component arounf 0 km s^{-1} can be associated with the central core region where number density is highest. The second component belongs to the density bump at $z = 0.07$ pc.

the majority of line profiles are not blue asymmetric (excepting HCN), but either red asymmetric or ambiguous. We also see that the fraction of blue asymmetric line profiles increases when going to higher transitions, and the fraction of red asymmetric line profiles decreases. The number of ambiguous line profiles is approximately constant. The mean and median values tend to become more negative at higher transitions. This is illustrated in Figs. A.1 - A.3 in the Appendix. These plots show histograms of derived δv at each transitions of HCN, HCO^+ and CS using N_2H^+ (1-0) as reference line.

Considering the whole sample, the maximal number of blue asymmetric spectra is detected at (5-4) transition (78.7%). This is the transitions at which the detection rate is highest for HCO^+ (83.3%) and CS (72.2%). In the case of HCN the greatest fraction of blue asymmetric line profiles (88.9%) is detected with the (4-3) transition.

Regardless of at which transition we observe the core the line profiles are never solely blue asymmetric. For the moment we can only state that the reliability increases with increasing transition. We will discuss the reasons for this later in Sect. 3.3.

We also considered whether these results might be influenced by the level of microturbulence in the gas. To study this is more details, we repeated the calculations introduced above and varied the amount of microturbulence, which has been initially 90 cm s^{-1}, between 50 cm s^{-1} and 3,000 cm s^{-1}. However, there is a lack of evidence that this variation has any significant impact on the fraction of observed blue asymmetric spectra. Therefore we will continue our further investigations with a microturbulence of 90 cm s^{-1}.

3.2.1 Dependency on the Reference Line

Before we continue our analysis we discuss how δv depends on the used reference line. For this we repeat the analysis above using N_2H^+, ^{13}CO and $H^{13}CO^+$ (3-2). These lines have the advantages that they are still bright enough to be clearly detected above the noise (see Table 3.5) and are probably less optically thick than the (1-0) transitions (see Sect. 3.3.2).

The results are similarly given as in Tables 3.2 - 3.4, Fig. 3.4 and Figs. A.4 - A.12 the above ones. In the case of N_2H^+ and $H^{13}CO^+$ (3-2) we see the same behaviour as before. At the lower transitions the fraction of total blue asymmetric line profiles is less than 50%. When going to higher transitions the fractions increases continuously up to 80.6% (N_2H^+ (3-2)) and 83.3% ($H^{13}CO^+$ (3-2)). Correspondingly, the mean and median values of derived δv become more negative. The fraction of red asymmetric line profiles decreases as the transition increases. Again the number of ambiguous line profiles is approximately constant. Thus, we improve our reliability, even if only slightly,

by using either N_2H^+ (3-2) or $H^{13}CO^+$ (3-2) as references. In the case of CS the number of line profiles classified as blue asymmetric increases significantly when making use of $H^{13}CO^+$ (3-2).

Unfortunately, using ^{13}CO (3-2) causes the opposite effect. Comparing the results with those using N_2H^+ (1-0) the numbers of blue asymmetric line profiles are smaller than before (maximal 63.9%). The distributions of δv (see Fig. A.7 - A.9) are still wide at higher transitions. Although the number of red asymmetric line profiles decreases, the fraction of ambiguous line profiles become larger. The mean δv values are even positive at (2-1) transitions of HCO^+ and CS.

Going to higher transitions not only increases the reliability of observing a blue asymmetric profile from a collapsing core when applied on optically thick tracers, but also when applied on optically thin reference lines. As CS and ^{13}CO have shown, not all tracers are equally well suited for such studies. The best results are gained when using $H^{13}CO^+$ (3-2) as a reference line, even if the results here differ slightly from those derived with N_2H^+ (1-0) or (3-2). In contrast, using ^{13}CO (3-2) worsens the results dramatically due to already mentioned effects of depletion that we did not considered in our analysis. We expect that the results conducted with ^{13}CO would improve if freeze out processes are included since disturbing factors by optical depth effects would decrease.

3.3 Origin of Emission Features

We have already seen, for example in Figs. 3.1 and 3.3, that the line profiles do not necessarily meet our expectations. Either there are additional components in the line profiles or the line profiles do not have the "right" asymmetry. An observer observing such spectra can only make educated guesses where these components come from and how they can use them to learn more about the structure and motions in the observed regions.

We are in the lucky situation that we know what is happening in the cores and that they will form sink particles in the future. This is an ideal opportunity to investigate where the disturbing components come from and to what extent the underlying processes wield influence. We will do this by studying the density, velocity and optical depth distributions.

tracer	transition	mean δv	median δv	blue	ambiguous	red
		km s^{-1}		%		
HCN	(1-0)	0.00821	-0.341	52.8	5.56	41.7
	(2-1)	-0.298	-0.731	58.3	13.9	27.8
	(3-2)	-0.718	-0.822	77.8	13.9	8.33
	(4-3)	-0.625	-0.598	88.9	5.56	5.56
	(5-4)	-0.586	-0.543	80.6	13.9	5.56
HCO^+	(1-0)	0.0504	0.163	38.9	11.1	50.0
	(2-1)	-0.0549	0.00	47.2	8.33	44.4
	(3-2)	-0.483	-0.798	66.7	11.1	22.2
	(4-3)	-0.499	-0.618	72.2	16.7	11.1
	(5-4)	-0.656	-0.681	83.3	11.1	5.56
CS	(1-0)	0.0504	0.00	41.7	19.4	38.9
	(2-1)	-0.0669	0.00	44.4	22.2	33.3
	(3-2)	-0.202	-0.230	55.6	19.4	25.0
	(4-3)	-0.371	-0.398	69.4	22.2	8.33
	(5-4)	-0.302	-0.284	72.2	25.0	2.78

Table 3.1: Summary of δv analysis using N_2H^+ (1-0) as a reference line. The columns show the mean and median values of δv and the fraction of blue, ambiguous and red asymmetric line profiles. The total number per transition is 36.

tracer	transition	mean δv	median δv	blue	ambiguous	red
		km s^{-1}		%		
HCN	(1-0)	0.175	-0.115	52.8	5.56	41.7
	(2-1)	-0.199	-0.766	58.3	13.9	27.8
	(3-2)	-0.711	-0.917	80.6	11.1	8.33
	(4-3)	-0.532	-0.565	88.9	2.78	8.33
	(5-4)	-0.501	-0.539	83.3	5.56	11.1
HCO^+	(1-0)	0.304	0.304	38.9	11.1	50.0
	(2-1)	0.168	0.00	47.2	8.33	44.4
	(3-2)	-0.447	-0.697	66.7	11.1	22.2
	(4-3)	-0.456	-0.610	72.2	13.9	13.9
	(5-4)	-0.608	-0.665	83.3	8.33	8.33
CS	(1-0)	0.215	0.00	33.3	19.4	47.2
	(2-1)	0.127	0.00	44.4	19.4	36.1
	(3-2)	-0.111	-0.0361	55.6	19.4	25.0
	(4-3)	-0.293	-0.468	72.2	11.1	16.7
	(5-4)	-0.225	-0.212	75.0	19.4	5.56

Table 3.2: Summary of δv analysis using N_2H^+ (3-2) as a reference line. As in Table 3.1.

tracer	transition	mean δv	median δv	blue	ambiguous	red
		km s^{-1}			%	
HCN	(1-0)	-0.0241	-0.298	52.8	5.56	41.7
	(2-1)	-0.407	-0.982	58.3	13.9	27.8
	(3-2)	-1.01	-1.24	83.3	8.33	8.33
	(4-3)	-0.832	-0.841	91.7	2.78	5.56
	(5-4)	-0.805	-0.907	88.9	8.33	2.78
HCO^+	(1-0)	0.0905	0.138	38.9	11.1	50.0
	(2-1)	-0.0373	0.00	47.2	8.33	44.4
	(3-2)	-0.677	-0.998	66.7	11.1	22.2
	(4-3)	-0.672	-1.04	75.0	13.9	11.1
	(5-4)	-0.904	-0.990	86.1	8.33	5.56
CS	(1-0)	0.0718	0.00	41.7	19.4	38.9
	(2-1)	-0.0982	0.00	47.2	16.7	36.1
	(3-2)	-0.273	-0.235	55.6	19.4	25.0
	(4-3)	-0.525	-0.779	80.6	8.33	11.1
	(5-4)	-0.435	-0.580	77.8	13.9	8.33

Table 3.3: Summary of δv analysis using $H^{13}CO^+$ (3-2) as a reference line. As in Table 3.1.

tracer	transition	mean δv	median δv	blue	ambiguous	red
		km s^{-1}			%	
HCN	(1-0)	0.0853	0.00	47.2	8.33	44.4
	(2-1)	-0.151	-0.388	52.8	19.4	27.8
	(3-2)	-0.405	-0.482	69.4	22.2	8.33
	(4-3)	-0.368	-0.301	75.0	19.4	5.56
	(5-4)	-0.265	-0.155	52.8	41.7	5.56
HCO^+	(1-0)	0.130	0.00	38.9	13.9	47.2
	(2-1)	0.0489	0.00	41.7	13.9	44.4
	(3-2)	-0.249	-0.432	63.9	13.9	22.2
	(4-3)	-0.266	-0.196	63.9	25.0	11.1
	(5-4)	-0.354	-0.291	75.0	22.2	2.78
CS	(1-0)	0.0291	0.00	33.3	38.9	27.8
	(2-1)	0.00153	0.00	44.4	22.2	33.3
	(3-2)	-0.0850	0.00	47.2	30.6	22.2
	(4-3)	-0.156	0.00	41.7	47.2	11.1
	(5-4)	-0.0311	0.00	27.8	58.3	13.9

Table 3.4: Summary of δv analysis using ^{13}CO (3-2) as a reference line. As in Table 3.1.

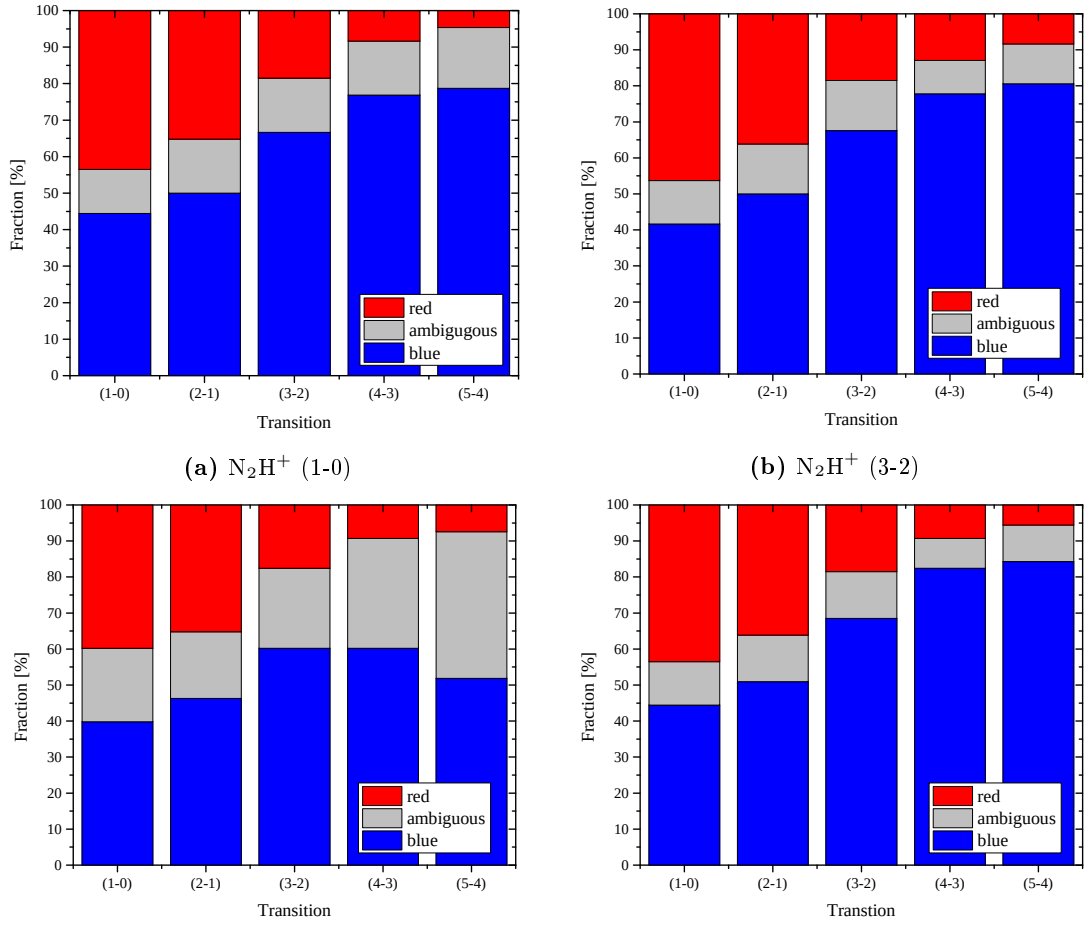

(a) N_2H^+ (1-0)

(b) N_2H^+ (3-2)

(c) ^{13}CO (3-2)

(d) $H^{13}CO^+$ (3-2)

Figure 3.4: Chart bars summarising the results of δv analysis. The graphs give the fractions of blue, red asymmetric or ambiguous line profiles at each transitions for all optically thick tracers, cores and sight-lines. The total number per transition is 108. The optically thin species and transitions which have been used as references are given in the corresponding captions. With increasing transition the numbers of blue line profiles increase, as the numbers of red asymmetric line profiles decreases. The fraction of ambiguous line profiles is almost constant.

3.3.1 Number Density – Velocity – Diagrams

It is intuitive to look first at how the gas is distributed in the cores and what the projected velocity components within the interesting regions are. For this purpose we plotted the number density and velocity distributions of molecular hydrogen along the line of sight z. We call these plots n - v - diagrams (cf. Sect. 2.3). Figs. 2.2 and 3.3 give two examples of such diagrams. The upper panel shows the velocity distribution, the lower panel the density distribution. The distributions are plotted with dashed lines. The thick black parts mark the dense regions where the number density becomes higher than 3×10^4 cm^{-3}. Red coloured regions show the dense gas which is within a radius of 0.05 pc, which roughly corresponds to the core radius around the core centre. Fig. 3.3 shows an example where both regions regions coincide.

But there are also cases where they do not, e.g. in Fig. 2.2. The dense gas distribution is still coherent. However, there is dense, emitting gas in front and behind what we defined as the core region. There is emission coming from the filaments around the core.

This effect becomes even more appreciable in examples like Figs. A.13 and A.14 in the Appendix. In Fig. A.13 there are two regions of dense gas, the first one is in front of the core region and the second one is located behind the core. In this example an observer could distinguish between both regions through their different observed velocity components (the core region at ~ 0 km s^{-1} and the background region around 4 km s^{-1}).

But this method would not work for cases as plotted in Fig. A.14. Here the second high-density region is in front of the core and the observed velocity is equal to the ones observed from the core region. Since the line profiles of optically thick tracers show only the gas at a certain velocity component which is closest to the observer. In this example it is foreseeable that an optically thick tracer is not going to show the line profile of the core, but the one of the filament in front of the core. In Fig. A.15 the corresponding line profile of HCN (1-0) is shown. The gas and velocity distributions results in the clear red asymmetry of the line profile. Since HCN (1-0) is optically thick (cf. Fig. A.16) the line profile is produced by out-flowing gas in the filaments, and NOT by the collapsing gas of the core. The latter is not visible to an observer due to the observation by the filament. This will be proved further in Sect. 3.3.2.

So far we have seen that n - v - diagrams can predict features in line profiles. We have also seen that this works also the other way around, if each velocity can be associated with a specific region with the system. In summary, n - v - diagrams are a very practical and helpful tool for identifying the origin of emission features in line profiles, as they are able to predict those. These are clear advantages, because the origins of odd features in

line profiles can be located, as well as the sources of non-blue asymmetric spectra.

However the disadvantage is also obvious. It is a purely theoretical method which can only be used for studies based on simulations where all three-dimensional positions and velocities are known. In particular when optical depth effects are taken into account it is impossible for observers to know how gas and velocity are distributed along the line of sight.

3.3.2 Optical Depth Surfaces

In observations only the plane perpendicular to the line of sight (here the x - y plane) can be mapped. Therefore, there is need for a tool which connects the theoretical n - v - diagrams with an observable map. Such a tool is given by the Optical Depth Surfaces (cf. Sect. 2.4).

`RADMC-3D` offers a function called `tausurf` which returns the three-dimensional position of where gas of given species at a given wavelength reaches a certain optical depth, τ, for the first time along the line of sight. In our case, we use $\tau = 1$ since we are interested in the position where our tracers become optically thick. Fig. 3.5 shows an example.

The plots consist of two components. he background shows the emission of a species at the corresponding transition in logarithmic scale. We do not want to go into more details about the morphologies of the cores, just give the reader a general idea of the gas distribution. The green star in the middle indicates the position of the core centre where the density peaks; this would correspond to the peak in dust emission. The colour scale in the foreground shows the surface returned by `tausurf` for $\tau = 1$. Here, positions with negative z are in front of the core ($z = 0$), and those with positive z behind it. The redder the colour scale (or the more negative z) the closer this position is to the observer.

The advantage of Optical Depth Surfaces is that they connect the observed maps (tracer emission, grey-scale) and line profiles with the theoretical n - v - diagrams. The n - v - diagrams have told us where the emitting gas is located and at which position we are going to see the emission in the spectrum. The Optical Depth Surfaces tell us which part of the emitted light we are actually able to observe, although this is still not possible for observers.

Optically Thick Tracers

In the case of HCO^+ (1-0) in Core B Fig. 3.5 shows that the majority of emission within the central region comes from the filaments in front (or behind) of the core and NOT from the core region itself. This explains why the corresponding line profile is red asymmetric.

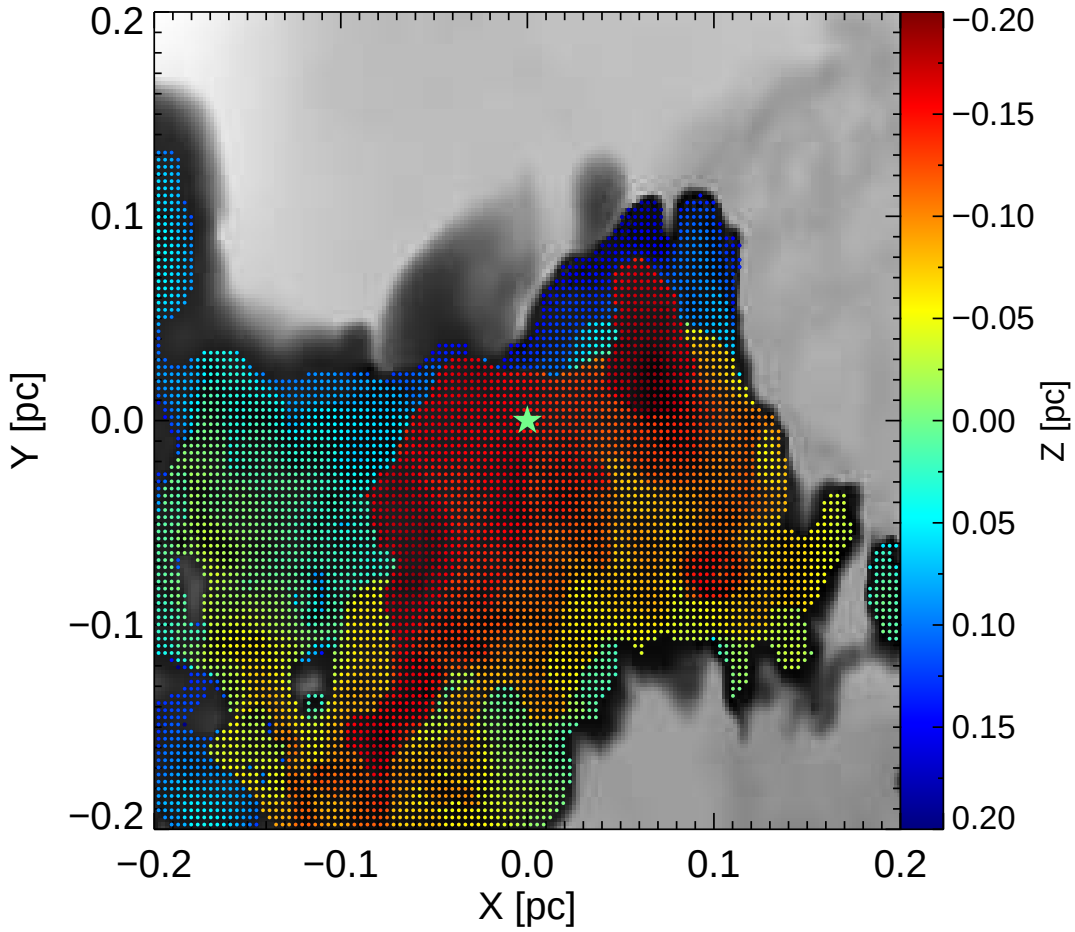

Figure 3.5: Optical depth surface plot. The grey-scale background shows the HCO^+ (1-0) emission in Core B at i =90° and ϕ =135°. The green star in the middle represents the core centre. The coloured points in the foreground indicates where the tracer (here HCO^+ 1-0) becomes optically thick. We see that the majority of the gas in front of the core is already optically thick.

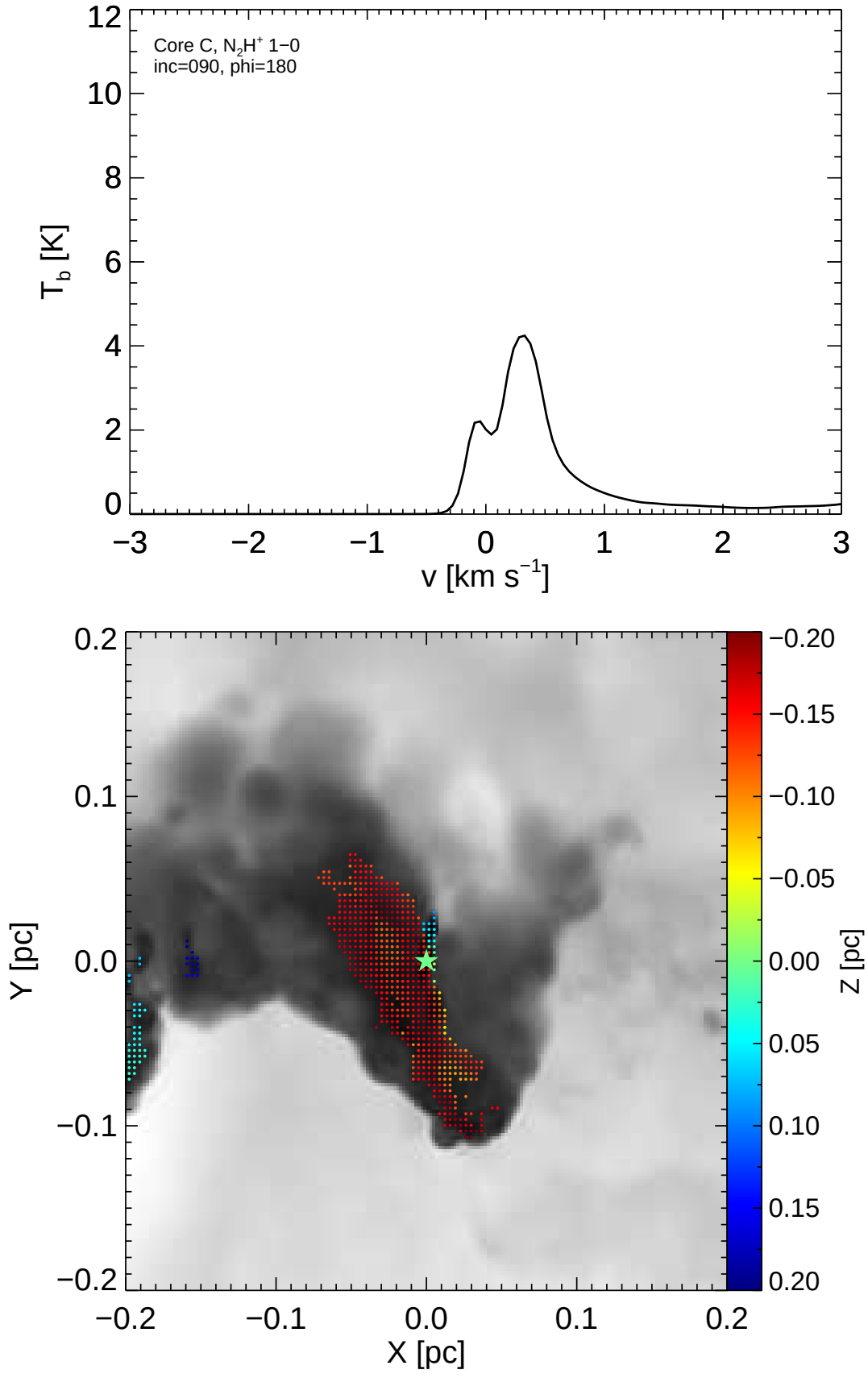

Figure 3.6: Line profile and optical depth surface of N_2H^+ in Core C at $i = 90°$ and $\phi = 180°$. The line profile is affected by self-absorption since N_2H^+ becomes optically thick within the observed area.

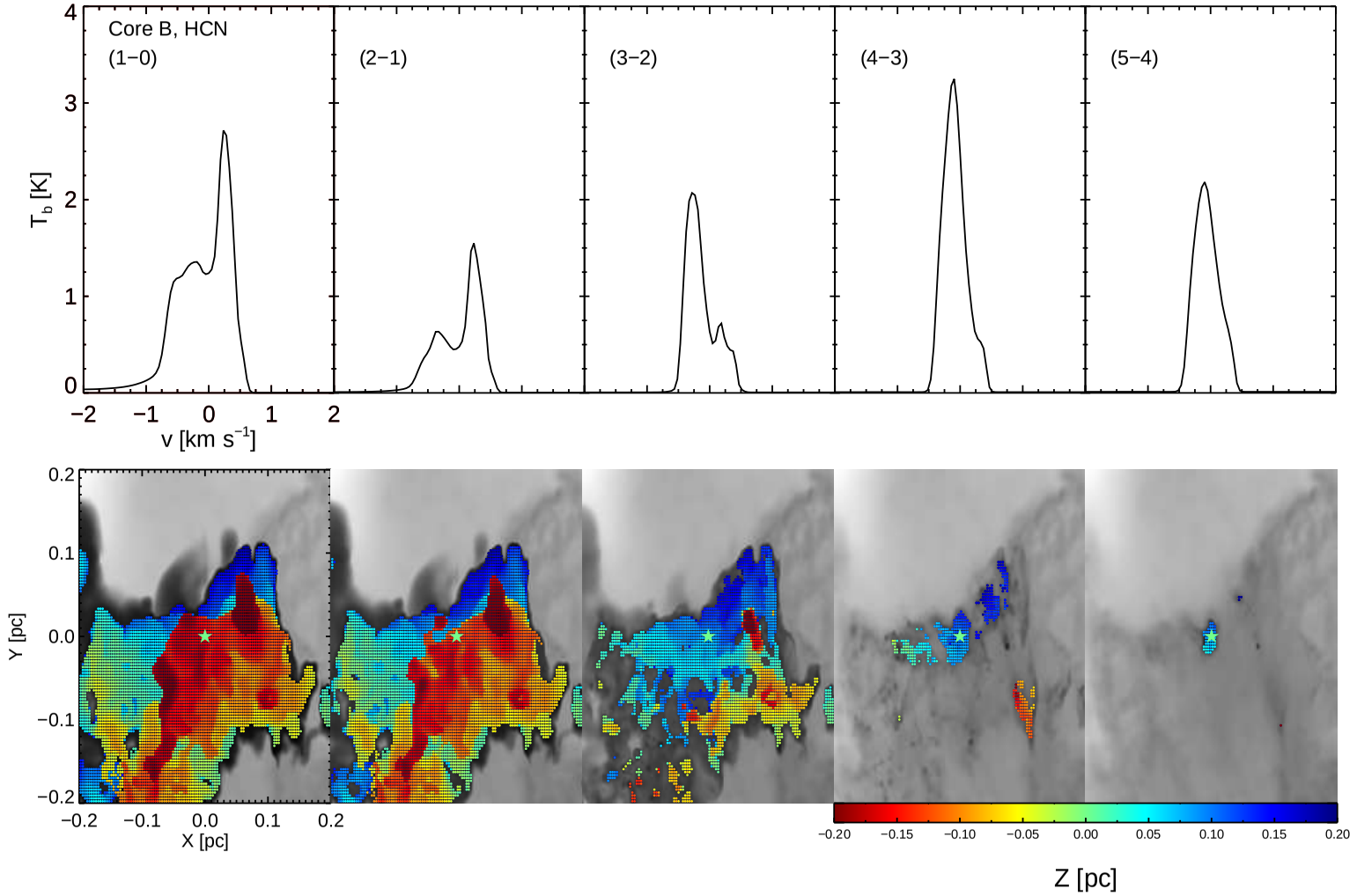

Figure 3.7: Line profiles and optical depth surfaces of HCN in Core B at $i = 90°$ and $\phi = 135°$. *Upper panel:* line profiles of HCN (1-0) to (5-4). *Lower panel:* corresponding optical depth surfaces. The areas of optically thick HCN becomes smaller at higher transitions (due to higher densities needed to populate these energy levels) and more closer to the core. At the same time the line asymmetry becomes bluer until the red peak transforms into a shoulder to the blue peak.

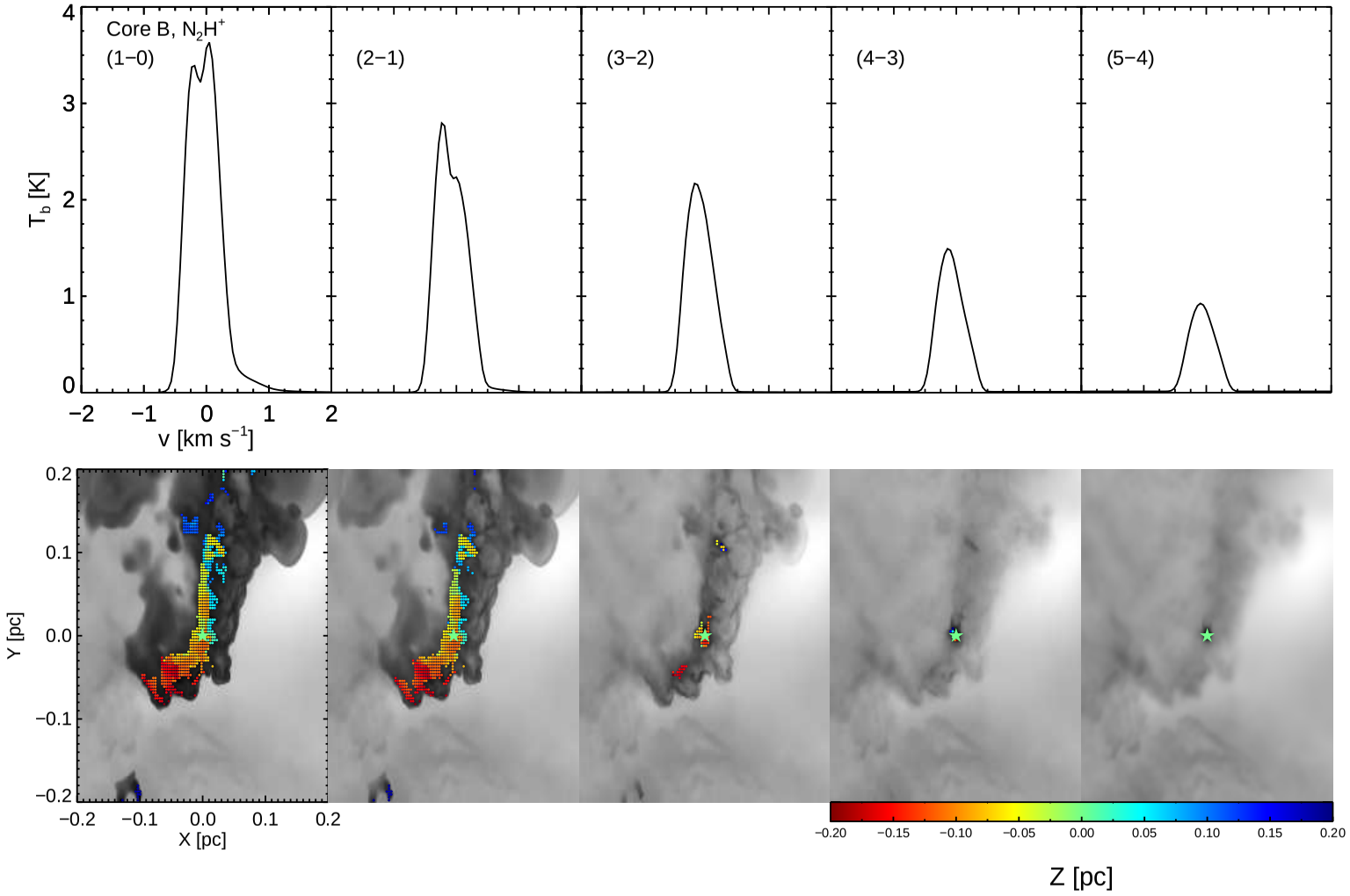

Figure 3.8: Line profiles and optical depth surfaces of N_2H^+ in Core B at $i = 0°$ and $\phi = 0°$. *Upper panel:* line profiles of N_2H^+ (1-0) to (5-4). *Lower panel:* corresponding optical depth surfaces. At low transitions N_2H^+ is optically thick and its line profiles are affected by self-absorption. At higher transitions N_2H^+ thins out and the line profiles become more Gaussian shaped.

Coming back to the example in Sect. 3.3.1 where we discussed the origin of the red asymmetric line profile of HCN (1-0) in Core A (Fig. A.14 and A.15) we may now consult Fig. A.16. It shows the corresponding Optical Depth Surface. One sees that a huge fraction of the optically thick gas within the marked central region is actually located in front of the core or on its outer edge. Since both observed velocity components are equal the optically thick filament hides the core itself. Thus the red asymmetry is not caused by expanding or oscillating gas motions of the core, but from the dense gas of the filaments in front of the core.

Such results are common for all optically thick tracers at lower transitions. We also see that the areas of optically thick gas becomes smaller at higher transitions (due to higher densities needed to populate these energy levels) and closer to the core (see Fig. 3.7 and discussion below).

Optically Thin Tracers

Optical Depth Surfaces, in combination with n - v - diagrams, also help to understand the origin of optical depth effects in the line profile of tracers which were supposed to be optically thin (see Fig. 3.1). If a tracer is really optically thin, its optical depth should never reach $\tau = 1$, `tausurf` should return no position and the Optical Depth Surfaces should be empty.

Unfortunately, that is not the case here. Fig. 3.6 shows the line profile and Optical Depth Surface of N_2H^+ (1-0) in Core C. The line profile does not have a Gaussian shape, but a dip at central velocity due to self-absorption. Instead of being empty, the corresponding Optical Depth Surface proves that N_2H^+ becomes optically thick.

We see the same effect in $H^{13}CO^+$ and ^{13}CO (1-0), too (cf. Fig. 3.1). This is a real problem since the optically thin species are needed as references of the δv analysis. Fitting a Gaussian to those line profiles causes large errors in central velocities.

Now we can use the Optical Depth Surfaces to explain the chanching asymmetries in the line profiles. Fig. 3.7 shows the line profiles and Optical Depth Surfaces of HCN (1-0) to (5-4) in Core B at $i = 90°$ and $\phi = 135°$. As has already been discussed the line profiles of HCN (1-0) and (2-1) are red asymmetric, but the higher ones blue asymmetric (or in the case of (5-4), approximately Gaussian due to optical thinness). In their corresponding Optical Depth Surfaces we see why this is so. In case of HCN (1-0) and (2-1) the majority of emission is coming from the filaments in front of the core region. At higher transitions this changes and the gas becomes optically thick behind the core centre.

It is still valid to expect blue asymmetric spectra in collapsing cores, even if they are non-spherical. To study this in more detail the filaments around the core would need to be removed and our investigates repeated. We, however, have learnt that the shape of line profiles can be influenced by dense gas which is located in filaments around the observed core. This is most obvious in the (1-0) and (2-1) transitions. For optically thick lines at higher transitions higher gas densities and population numbers are needed for substantial emission. Thus, the observer is able to look through the filaments, focus on the core region and study what is really going on there.

In a similar fashion going to higher transitions works also for our reference lines. Fig. 3.8 shows this with the example of N_2H^+ in Core B at $i = 0°$ and $\phi = 0°$. In the line profiles of N_2H^+ (1-0) and (2-1) we see that the lines are not Gaussian shaped, but affected by self-absorption. The corresponding Optical Depth Surfaces below them prove that. When going to higher transitions the gas soon becomes optically thinner and the line profiles more Gaussian shaped.

Similar to the classification of line profiles discussed before it is not really effective for large samples to look at each Optical Depth Surface. Analogously to the normalised velocity difference the results of `tausurf` can be used for more quantitative analysis.

Figs. 3.9, 3.10, 3.11 show histograms of `tausurf` results for HCN, HCO^+ and CS. Each figure contains five histograms, one for each transition. The histograms show the positions where the gas becomes optically thick for the first time along the line of sight within the region covered by the beam (FWHM = 0.01 pc). The numbers are for all cores and sight-lines. Positions of both mean and median of the distributions are marked, as well.

In all three figures one sees the same behaviour. In the (1-0) transition the distributions are flat and wide ranged. The same is true for (2-1). Then beginning with (3-2) the distributions become more peaked and narrow. The positions of the peaks are usually in front of the core centre. The higher the transition, the greater the peak and the narrower the distributions. We also see that the mean and median positions are outside the core region at (1-0), except of CS (1-0). When going to higher transitions both increasingly approach the core centre.

In the lower transitions the optically thick gas is widely distributed and not centred within the core region. We not only see that the filaments contain a lot of dense gas, but also that this gas is to a great extent optically thick. Consequently the filaments prevent the observer from observing the line profile of the core. Instead the observer sees the line profiles of the filaments which are not collapsing onto the core. At higher transitions, beginning in the (4-3) transitions, where higher densities are needed to populate the

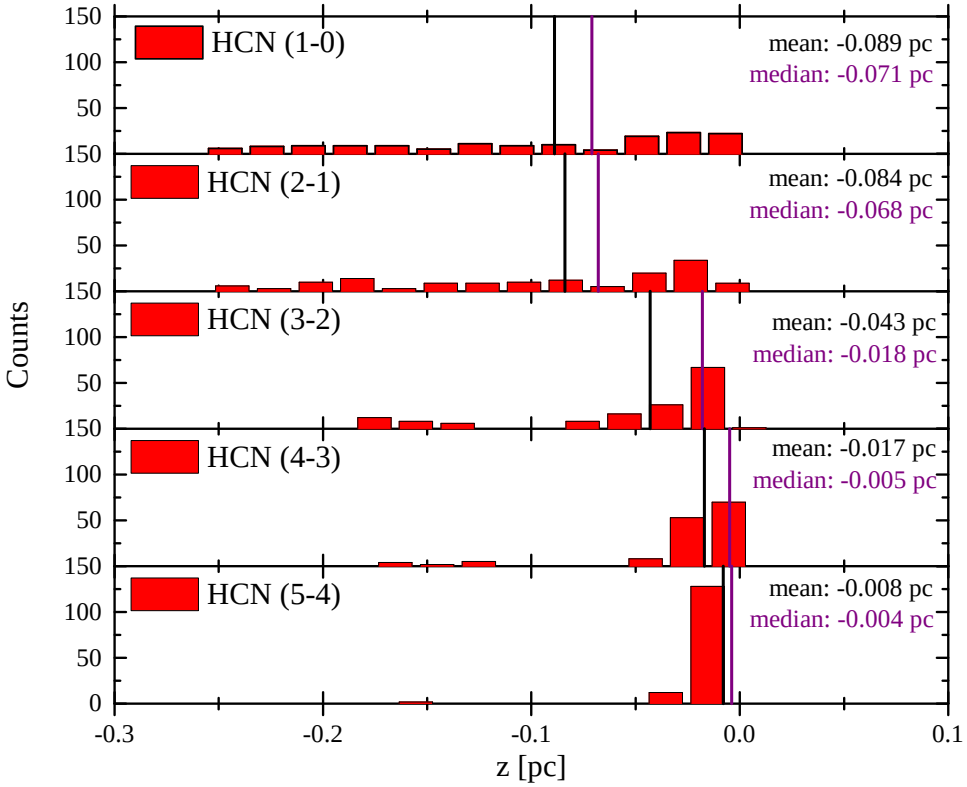

Figure 3.9: Histograms of results of optical depth surface analysis of HCN. The histograms show the positions where the emission transitions of HCN becomes optically thick along the line of sight z. Negative z are in front of core according to the observer, positive z behind the core. The core centre is at $z = 0$. The numbers are summed up for all cores. Average (black) and median (violet) positions are also given. The histograms show that the regions with optically thick gas are distributed closer to the core when going to higher transitions, as well as the distributions become narrower.

levels, the gas in the filaments become optically thin and the core is revealed. Now the observer is able to observe the line profiles of the collapsing gas.

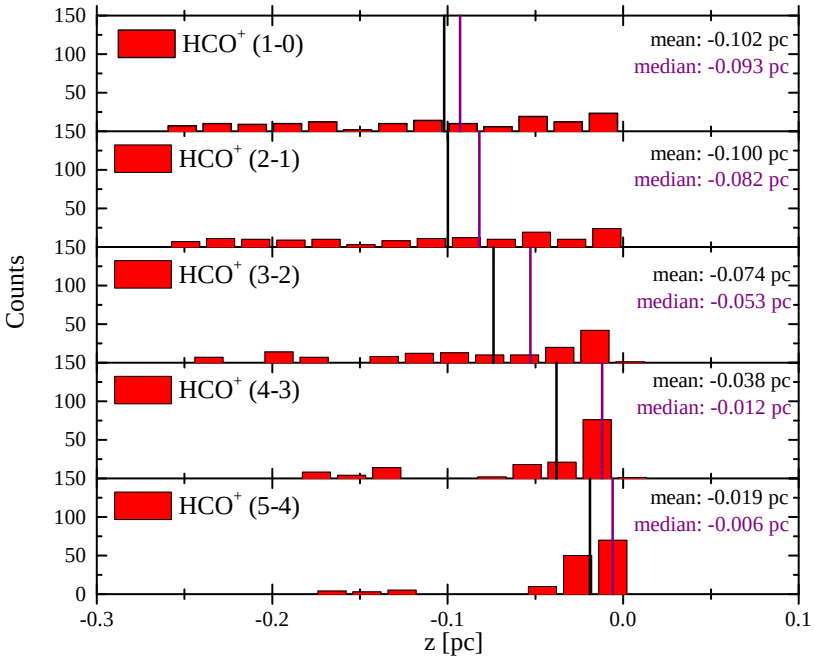

Figure 3.10: Histograms of results of optical depth surface analysis of HCO^+. As in Fig. 3.9.

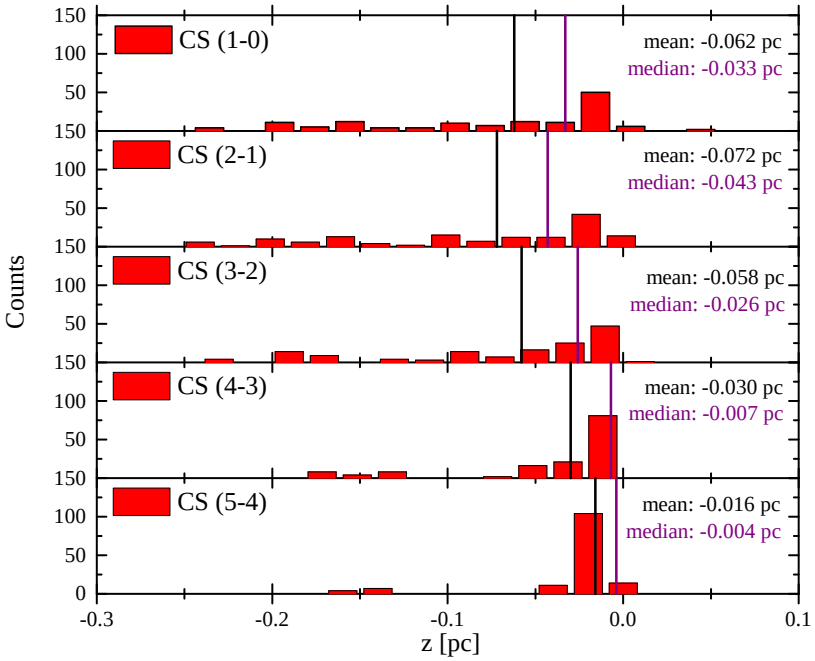

Figure 3.11: Histograms of results of optical depth surface analysis of CS. As in Fig. 3.9.

tracer	transition	mean T_b	min T_b	median T_b	max T_b
		K		K	
HCN	(1-0)	4.3	1.3	4.3	10.3
	(2-1)	3.3	0.8	3.3	10.9
	(3-2)	3.1	0.9	2.9	5.8
	(4-3)	3.0	1.4	3.0	5.2
	(5-4)	2.3	1.0	2.0	4.1
HCO^+	(1-0)	6.1	2.4	5.7	13.6
	(2-1)	4.8	1.0	4.4	11.5
	(3-2)	4.6	1.5	4.5	10.1
	(4-3)	3.9	1.8	3.6	8.2
	(5-4)	3.4	1.6	3.2	6.3
CS	(1-0)	6.2	3.0	5.5	12.9
	(2-1)	5.0	2.4	4.5	10.8
	(3-2)	4.4	1.5	3.9	9.8
	(4-3)	4.1	1.9	4.1	8.2
	(5-4)	3.8	2.1	4.0	7.1
N_2H^+	(1-0)	4.1	2.9	4.1	5.3
	(2-1)	3.1	1.9	3.2	4.4
	(3-2)	2.5	1.9	2.4	3.3
	(4-3)	1.8	1.5	1.7	2.2
	(5-4)	1.0	0.9	1.0	1.3
$H^{13}CO^+$	(1-0)	2.1	1.1	2.4	3.2
	(2-1)	2.0	1.5	2.0	2.3
	(3-2)	1.5	1.2	1.4	1.7
	(4-3)	0.8	0.7	0.8	1.0
	(5-4)	0.4	0.3	0.4	0.5
^{13}CO	(1-0)	8.8	7.4	8.6	10.5
	(2-1)	6.4	4.4	6.4	8.1
	(3-2)	4.9	3.4	4.7	6.4
	(4-3)	3.9	3.2	3.8	4.8
	(5-4)	3.0	2.4	2.9	3.5

Table 3.5: Summary of measured brightness temperatures. The table gives the average values of brightness temperatures. For error estimations minimal, maximal and median values are provided. In the case of optically thick tracers the given values of brightness temperature correspond to the higher peak in asymmetric line profiles. If the line profiles are classified as ambiguous, both peak brightness temperatures were considered.

3.4 Observational Considerations

So far, we have ignored observational limitations in the analysis. Real observed line profiles are not only affected by optical depth effects along the line of sight, but also by noise, limited resolutions, and many more. In this section we want to investigate the influence of noise on the line asymmetry analysis.

Noise is a constant problem in observational astronomy, especially if weak lines are supposed to be observed. We have stated before that the fraction of detected blue asymmetric line profiles in dense star-forming clusters within filamentary becomes higher with higher transitions of used tracers. But the higher the transition the weaker the observed line. Table 3.5 summarises the intensities of our simulated lines. We see that there are huge differences between minimal and maximal detected brightness temperature in each transitions, depending on the line of sight-angle at which one looks at the cloud. On average, the mean brightness temperatures of (1-0) transitions are between 1 and 14 K. Going to higher transitions the brightness temperatures become weaker until the mean brightness temperatures are just between 0.3 and 2.4 K in (5-4) transitions.

An average of typical noise level in star-forming regions is about 0.18 K (corresponding to 50 mJy, Schuller et al. 2009). Of course, the real noise levels depend on many different factors, like the used instruments, the conditions during the observations, the brightness of the source and so on. Here, we do not want to go into details on possible noise sources, but on how our results may be affected by noise effects.

All lines, which we used for our investigations, except for higher transitions of $H^{13}CO^+$ would be detectable above 5σ noise. Fortunately $H^{13}CO^+$ (3-2) is not affected by this problem and so we still suggest it as the optimal reference line.

Another problem of noise appears in the context of ambiguous line profiles. In the case of ambiguous line profiles the relative brightness temperature difference between the two peaks is less than 10% (cf. Sect. 2.2). Looking at our average brightness temperatures the differences would be between 0.1 and 1.4 K in (1-0) transitions and below 0.3 K in (5-4) transitions. These small differences are very sensitive to noise disturbances. As long as both lines are equally affected by noise effects, this might not be critical, but imagine the case that we have an ambiguous line profile and one of the peaks is significantly affected by noise that increases the observed brightness temperature. An example is shown in Fig. 3.12. We have simulated the noise by using the `IDL` function `randomn` which generates a normalised random distribution. The function has been called 200 times and the results have been averaged and calibrated to the wanted noise level (here, 0.18 K). The final noise distribution has been added to an ambiguous line profile

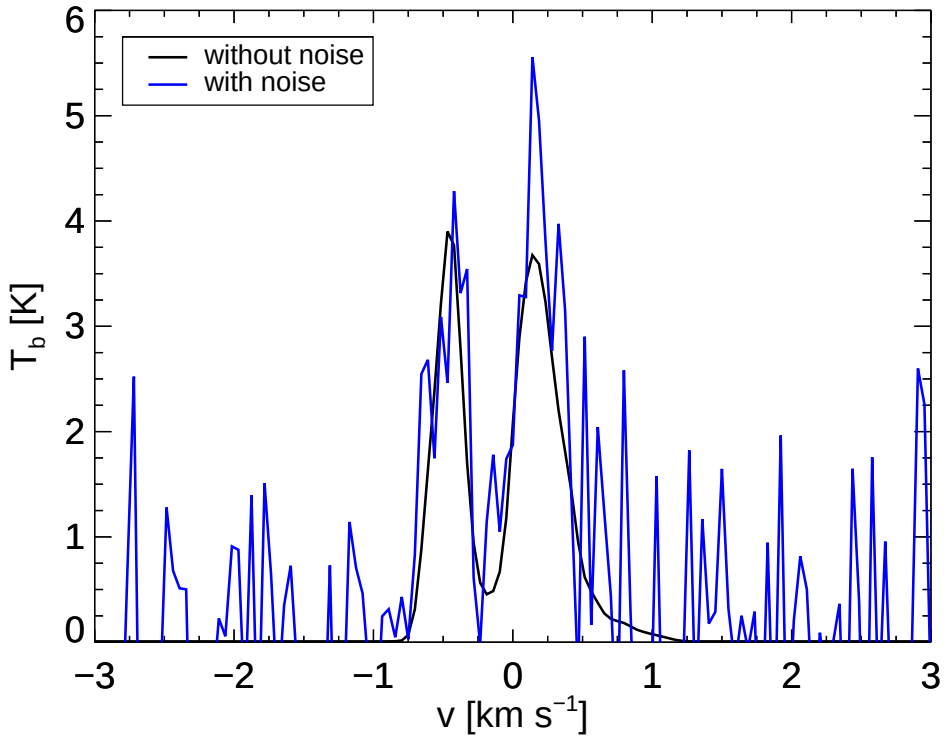

Figure 3.12: Example for the influence of noise on the classification of ambiguous line profiles. The black line shows the an exemplary ambiguous line profile of the HCN (3-2) transition in Core A at $i = 315°$ and $\phi = 0°$ without noise (see Fig. 1.5). The blue line shows the same line profile with noise which has been generated by adding a random, normalised noise distribution to the HCN line profile. The noise affected line profile seems to be red asymmetric.

(which has already been shown in Fig. 1.5). In such a case the difference between the peak brightness temperatures increases and might becomes greater than 10%. The line profile would be classified as asymmetric – we do not want to specify whether red or blue asymmetric – although is ambiguous. Though this will not be the rule, it is necessary to rephrase the peak brightness temperatures differences correlated criterion so that it bases on the noise level of the observed region. The goal is to introduce a criterion which can be applied in observational studies and return reliable results which are not (significantly) distorted by noise.

In this section we repeat the δv analysis conducted in Sect. 3.2, but use the following criteria for ambiguous line profiles:

1. $|T_{mb,1} - T_{mb,2}| < n \cdot \sigma$

2. $|v_{thick,1} - v_{thick,2}| < \Delta v_{thin}$

where σ represents the noise level in terms of temperatures (in this study $\sigma = 0.18$ K). n is an integer and represents the degree of significance one wants lines and brightness temperatures to be above the noise level. In observations lines are usually supposed to be detected if their brightness temperatures are above the 3σ noise level, also 5σ or 6σ noise levels are common. Therefore we use these three limits (3σ, 5σ, and 6σ) for our investigations.

Again we use the N_2H^+ (1-0), (3-2), $H^{13}CO^+$ (3-2) and ^{13}CO (3-2) lines as reference lines and the (1-0) to (5-4) transitions of HCN, HCO^+ and CS as optically thick tracers. Figs. 3.13, 3.14 and 3.15 show summary charts of the result when using the corresponding noise limit. In the charts the numbers of line profiles with detected blue, red and ambiguous asymmetries are summed up for all optically thick tracers and optically thin reference line such that the plotted fractions only depend on the transition of the optically thick species.

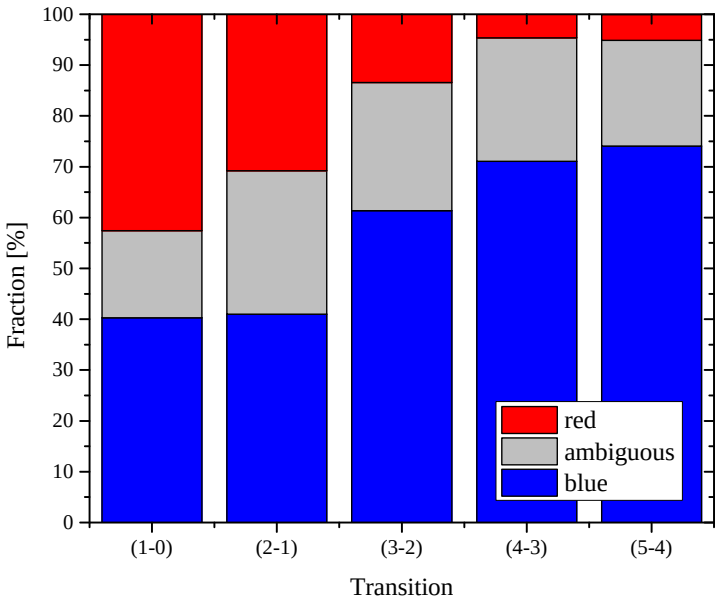

Figure 3.13: Chart bar summarising the results of δv analysis using a 3σ noise level as threshold. Analogously as in Fig. 3.4, but this chart bar sums up the results obtained with all optically thick, as well as optically thin reference lines (see Fig. A.17 fro more details). The chart bar shows again that the fraction of blue line profiles increases with increasing transition, as the numbers of red profiles decrease. The fraction of ambiguous line profiles has become large compared to the study without noise criterion.

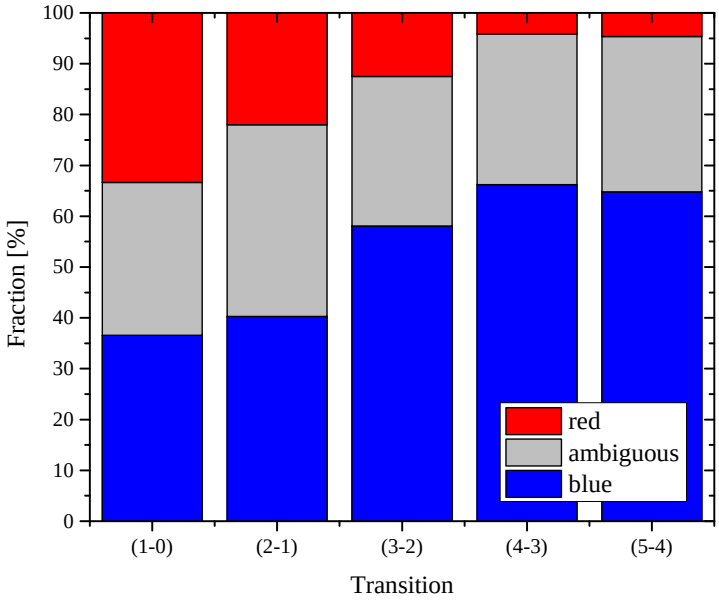

Figure 3.14: Chart bar summarising the results of δv analysis using a 5σ noise level as threshold (see Fig. A.18 fro more details). As in Fig. 3.13.

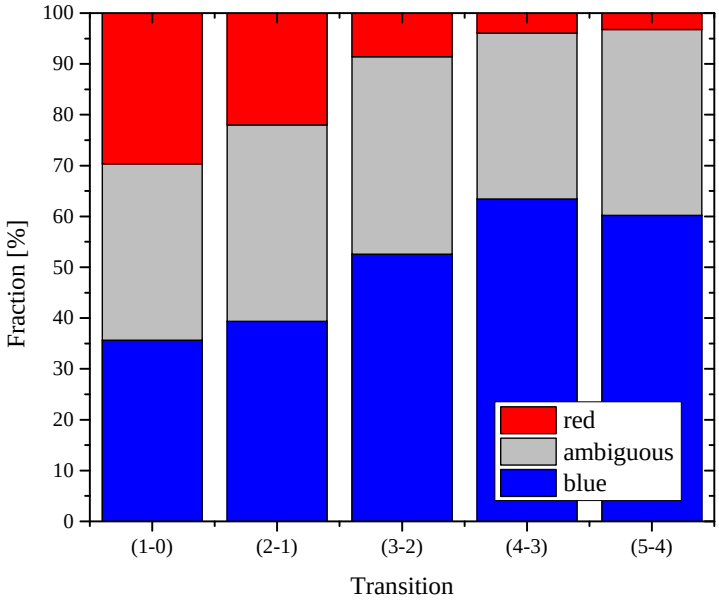

Figure 3.15: Chart bar summarising the results of δv analysis using a 6σ noise level as threshold (see Fig. A.19 fro more details). As in Fig. 3.13..

The figures show the same trends as in the studies before. In the (1-0) transitions the fraction of blue asymmetric spectra is on the order of 40% which increases up to 60-75% in the (5-4) transition. These numbers are about 5 - 10% lower than the numbers derived in Sect. 3.2. Similarly the total fraction of red asymmetric spectra decreases from ca. 40% in the (1-0) transitions down to 3 - 5% which is again less than in the study of Sect. 3.2. Consequently the total number of line profiles which are classified as ambiguous increases drastically by about 10% compared with the results before. This is easily understood by considering the first criterion for ambiguous line profiles again. When we used a relative temperature difference limit between the peaks of 10%, the temperature differences of detected (red or blue) asymmetries of weaker lines have been smaller than or on the same order of magnitude as the typical noise level. By introducing a noise dependent formulation of this criterion we increased the threshold and select only those line profiles with higher peak temperature differences and, thus, more obvious line profile asymmetries. The other spectra with peak differences between 10% T_{max} and $3/5/6\sigma$ are now classified as ambiguous. Hence, it is also intuitive that the fraction of ambiguous spectra becomes larger with higher n. In all transitions the numbers of ambiguous line profiles doubles when we use the 6σ threshold compared to the numbers derived with the 3σ limit. At the same time the numbers of blue and red asymmetric line profiles decreases with higher n, though not as rapidly as the numbers of ambiguous spectra increase.

In summary, rephrasing our first criterion for ambiguous spectra such that the minimal difference of peak brightness temperatures above which asymmetries of line profiles can clearly be classified depends on the noise level influences the results of δv analysis significantly. The numbers of spectra which are classified as ambiguous become larger due to decreasing numbers of blue and red asymmetric line profiles. This results seems to be worse than the results derived in Sect. 3.2, where we used a more theoretical ansatz, because as a consequence thereof the gas motions within the core regions are observationally worse identified. But a lower number of red asymmetric line profiles means also a lower number of "false" detections which improves the general outcome of the analysis. Furthermore, these results are more realistic to be adapted into and compared to observational studies. Additionally, they are in good agreement with existing studies, for example, Gregersen et al. (1997), Gregersen & Evans (2000), André et al. (2007) and Sohn et al. (2007).

4 Summary & Conclusion

The goal of this thesis was to find an optimal, reliable tracer for collapsing cores in dense, filamentary clusters. For this, we continued the analysis of Smith et al. (2012) and investigated the question of whether blue infall line profiles are expected in irregularly shaped, collapsing cores which are embedded in filaments.

Three cores were selected by Smith et al. (2012) out of a Giant Molecular Cloud simulation, because they were irregular, deeply embedded in filaments, already collapsing, and will form stars in the future. This biases the sample to real star-forming regions with complex density and velocity pattern. However, the analysis of Smith et al. (2012) was limited to only one optically thick and one optically thin transition. We addressed this limitation by modelling the (1-0) – (5-4) transitions of three optically thick tracers (HCN, HCO^+, CS) and three optically thin tracers (N_2H^+, $H^{13}CO^+$, ^{13}CO) at twelve different line of sight-angles assuming constant abundances. We used the δv method to classify the line profile asymmetries of optically thick tracers. We analysed the number density and velocity distributions of the cores and studied the distribution of optical thickness by using Optical Depth Surfaces, a function which returns the first point along the line of sight where the gas became optically thick.

We saw that blue asymmetric line profiles are expected in irregular cores, as they are in spherical cores. Although less than 50% of simulated line profiles were blue asymmetric in the (1-0) transitions, the fraction of blue line profiles increased when going to higher transitions of the optically thick tracers. We obtained our best results in the (4-3) transitions of HCN and HCO^+ where about 90% of the line profiles were blue asymmetric. The success rate from the (3-2) and (5-4) transitions was only marginally lower. However, these transitions are either, in case of (3-2), more affected by the surrounding filaments or, in case of (5-4), fainter, and therefore harder to observed. Thus, the (4-3) transition offers the best combination of detectability of blue line profiles and visibility above typical noise levels. This makes it the most reliable tracer for dense core gas motions in star-forming clusters. We confirmed this result by introducing classification criteria which toke observational conditions, like typical noise levels, into account. This method reduced the maximal fraction of blue asymmetric line profiles to 60% – 75% (depending on the chosen

threshold). However, the (4-3) transitions still produced the most reliable results.

Furthermore, we investigated the origin of "false" line profiles asymmetries by using the Optical Depth Surfaces. These were localised in the filaments around the cores where the gas is dense enough to become optically thick and hide the core behind. However, since higher transitions need higher number densities, the filaments thin out optically at higher transitions. Thus, the cores and their blue line profiles become detectable. In addition, the Optical Depth Surfaces showed that the optically thin tracers may become optically thick in the lower transitions. Since they were needed as reference lines in the δv analysis we also used higher transitions of the optically thin tracers to improve the analysis. The (3-2) transitions turned out to the best choice, since they were usually optically thin, bright and had central frequencies close to the (4-3) transitions of the optically thick tracers.

Neglecting depletion effects of carbon bearing species (CS and ^{13}CO in our study) led to great problems since it produced artificial high number densities, brightness temperatures and optical thicknesses in these cases. The results obtained with these two molecules need to be treated cautiously. Future investigations should consider the effects of depletion to be more comparable to observations.

In summary, blue infall line profiles are expected for irregular, collapsing cores. Non-blue asymmetric line profiles of optically thick tracers and non-Gaussian line profiles of optically thin tracers are caused by dense filaments around the cores along the line of sight. These effects can be avoided by using higher transitions for studies. The best results were obtained with the (4-3) transitions of the optically thick tracers while using the (3-2) transitions of optically thin tracers as reference lines. This approach is also applicable to observational studies, since the lines are still bright enough to be visible and are less influenced by the surrounding filaments than lower transitions.

Appendix

Additional Information

tracer	transition	frequence ν	wavelength λ	critical density n_{crit}
		GHz	μm	cm^{-3}
HCN	(1-0)	88.6316023	3382.45558	1.0073×10^6
	(2-1)	177.2611115	1691.24776	1.0316×10^7
	(3-2)	265.8864343	1127.5207	7.3297×10^7
	(4-3)	354.5054779	845.663824	3.1121×10^8
	(5-4)	443.1161493	676.555026	9.6979×10^8
HCO^+	(1-0)	89.188523	3361.3345	1.6351×10^5
	(2-1)	178.375065	1680.6859	1.0739×10^6
	(3-2)	267.557619	1120.4781	3.4319×10^6
	(4-3)	345.734288	840.38027	9.0673×10^6
	(5-4)	445.902996	672.32663	1.7250×10^7
CS	(1-0)	48.9909549	6119.34300	4.7273×10^5
	(2-1)	97.9809533	3059.70138	3.1683×10^5
	(3-2)	146.9690287	2039.83425	1.2648×10^6
	(4-3)	195.9542109	1529.91077	2.5729×10^6
	(5-4)	244.9355565	1223.96463	8.0557×10^7
N_2H^+	(1-0)	93.173700	3217.56524	1.5774×10^5
	(2-1)	168.344771	1608.80531	9.4100×10^5
	(3-2)	279.511701	1072.55781	2.9967×10^6
	(4-3)	372.672509	804.439423	7.7313×10^6
	(5-4)	465.824947	643.573213	1.5061×10^7
$H^{13}CO^+$	(1-0)	86.7542884	3455.65001	1.6754×10^5
	(2-1)	173.5066953	1727.84374	9.9965×10^5
	(3-2)	260.2553390	1151.91665	3.1843×10^6
	(4-3)	346.9983381	863.95935	8.2198×10^6
	(5-4)	433.7338110	691.18997	1.6016×10^7
^{13}CO	(1-0)	110.201354	2720.406296	1.90631×10^3
	(2-1)	220.398684	1360.228000	8.4448×10^3
	(3-2)	330.587965	906.846250	2.7448×10^4
	(4-3)	440.765173	680.163670	6.5972×10^4
	(5-4)	550.926285	544.160756	1.6283×10^5

Table A.1: Detailed list of frequences, wavelengths and critical densities for each tracer and transition. The critical densities are given for LTE and are estimated by $n_{crit} = A_{ul} \,/\, K_{ul}$ where A_{ul} represents the Einstein coefficient and K_{ul} the collisional rate coefficient at a temperature of 20 K.

Additional Figures

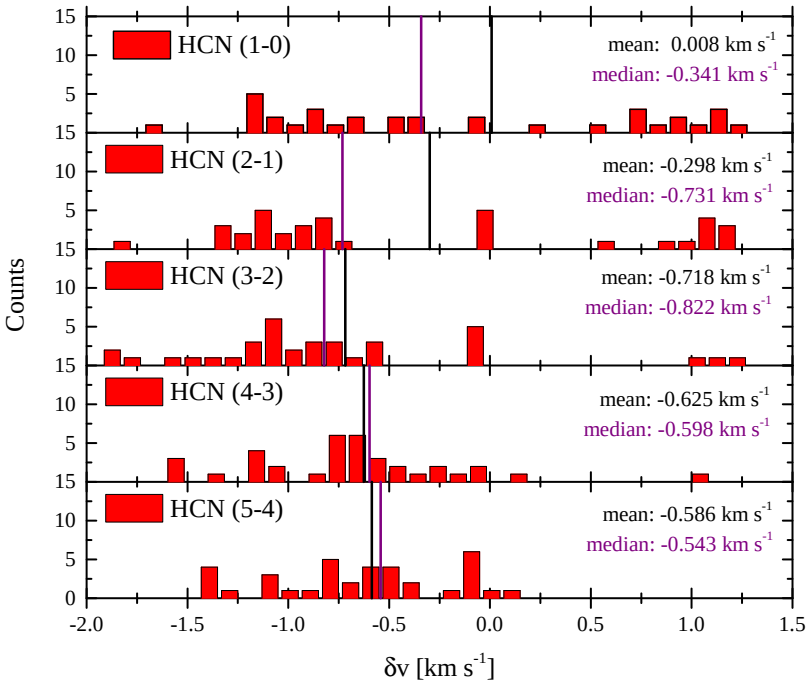

Figure A.1: Histogram of HCN δv results using N_2H^+ (1-0) as reference line. Going to higher transitions the distributions become narrower and the mean and median values of δv more negative.

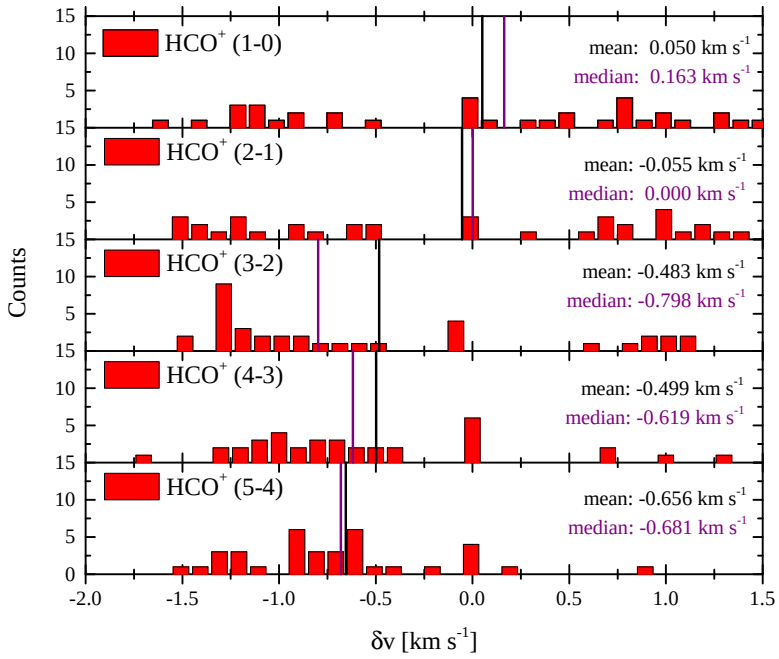

Figure A.2: Histogram of HCO^+ δv results using N_2H^+ (1-0) as reference line. As in Fig. A.1.

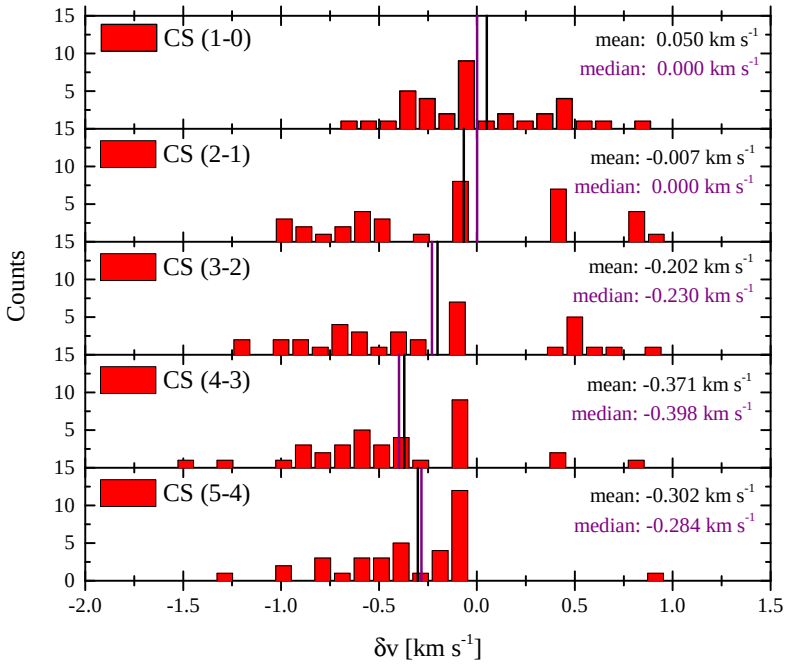

Figure A.3: Histogram of CS δv results using N_2H^+ (1-0) as reference line. As in Fig. A.1.

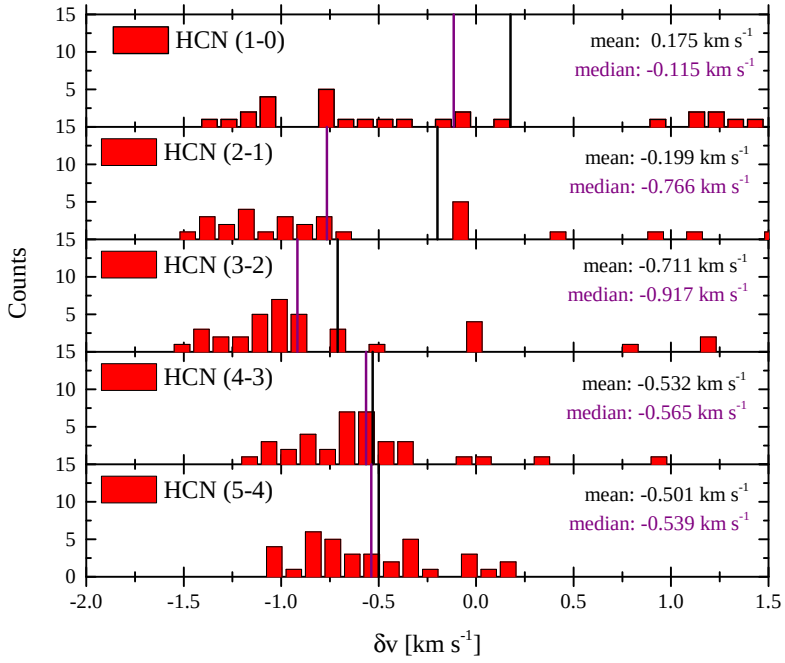

Figure A.4: Histogram of HCN δv results using N_2H^+ (3-2) as reference line. As in Fig. A.1.

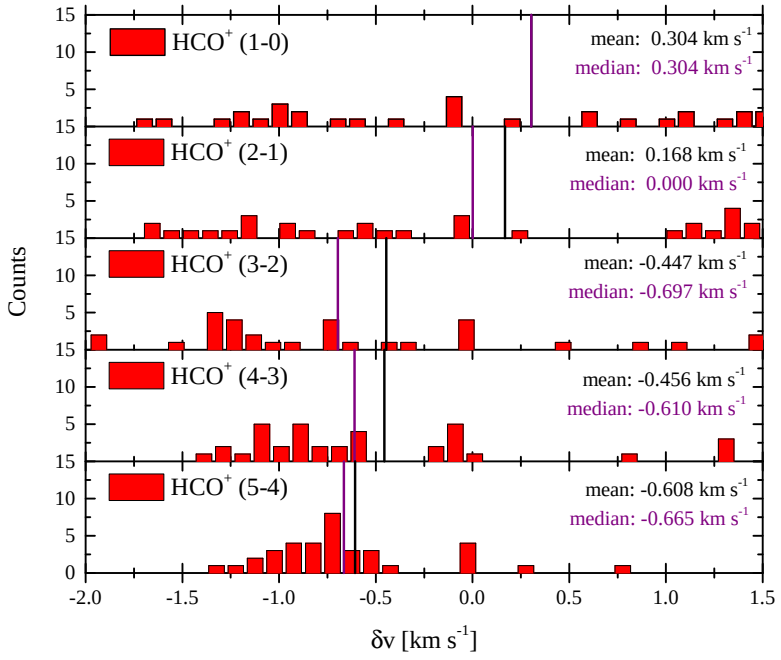

Figure A.5: Histogram of HCO^+ δv results using N_2H^+ (3-2) as reference line. As in Fig. A.1.

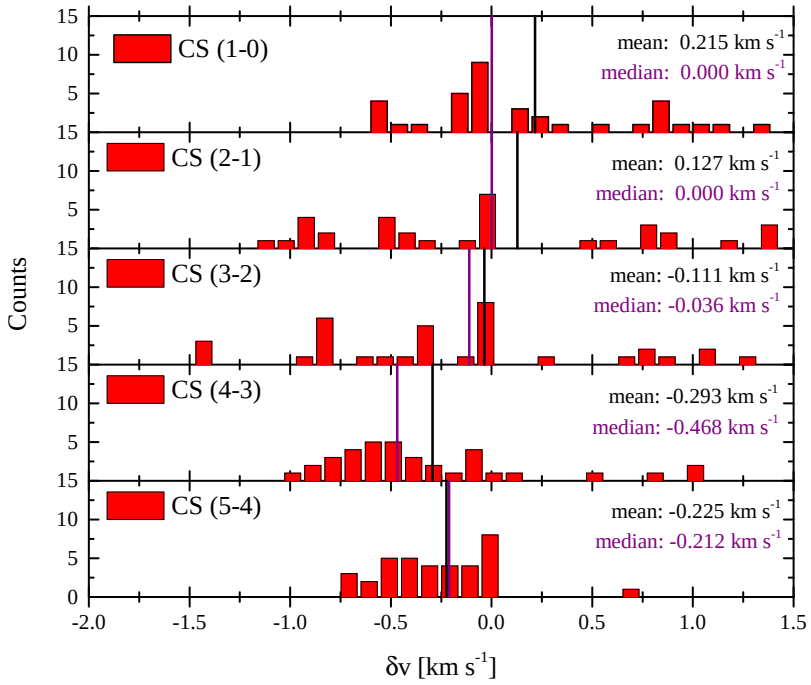

Figure A.6: Histogram of CS δv results using N_2H^+ (3-2) as reference line. As in Fig. A.1.

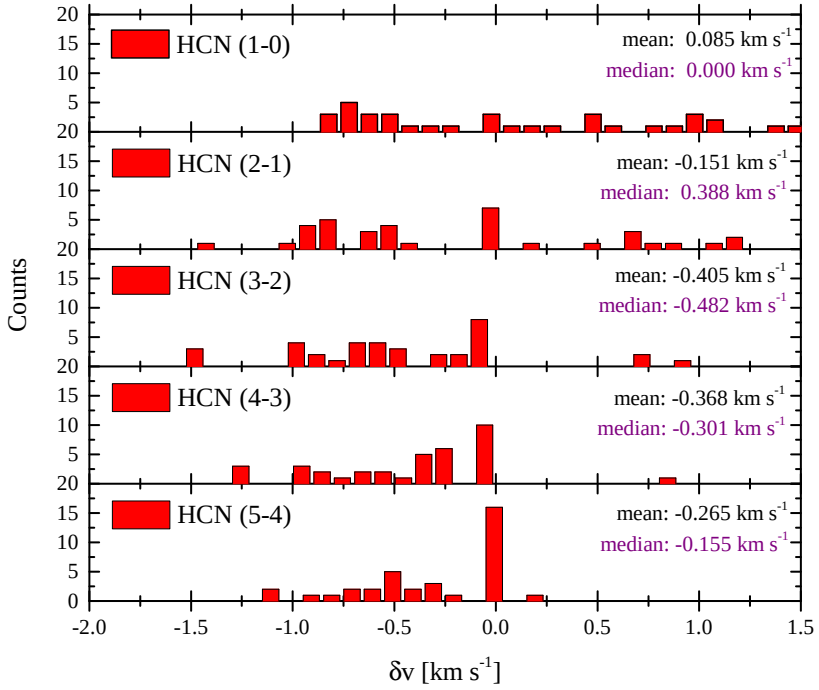

Figure A.7: Histogram of HCN δv results using ^{13}CO (3-2) as reference line. As in Fig. A.1.

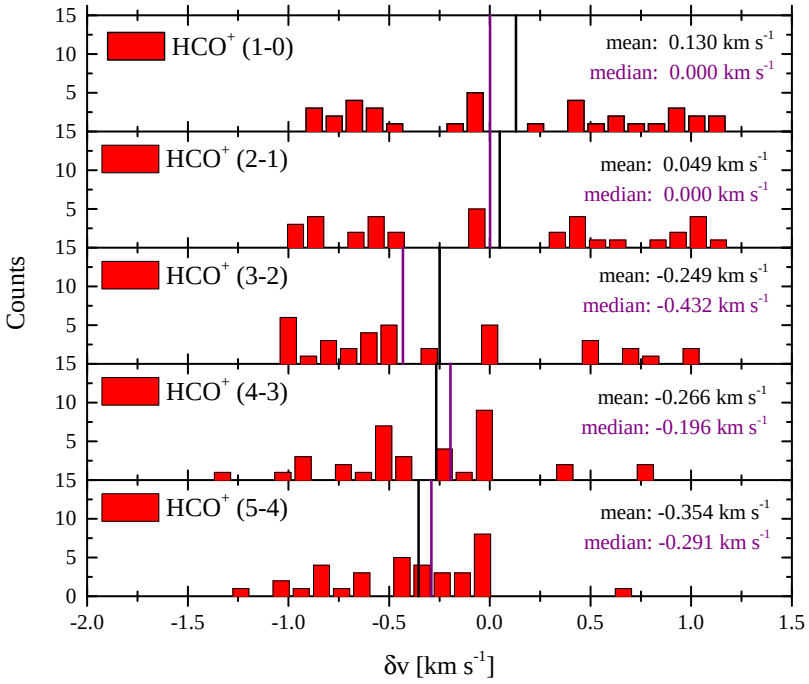

Figure A.8: Histogram of HCO^+ δv results using ^{13}CO (3-2) as reference line. As in Fig. A.1.

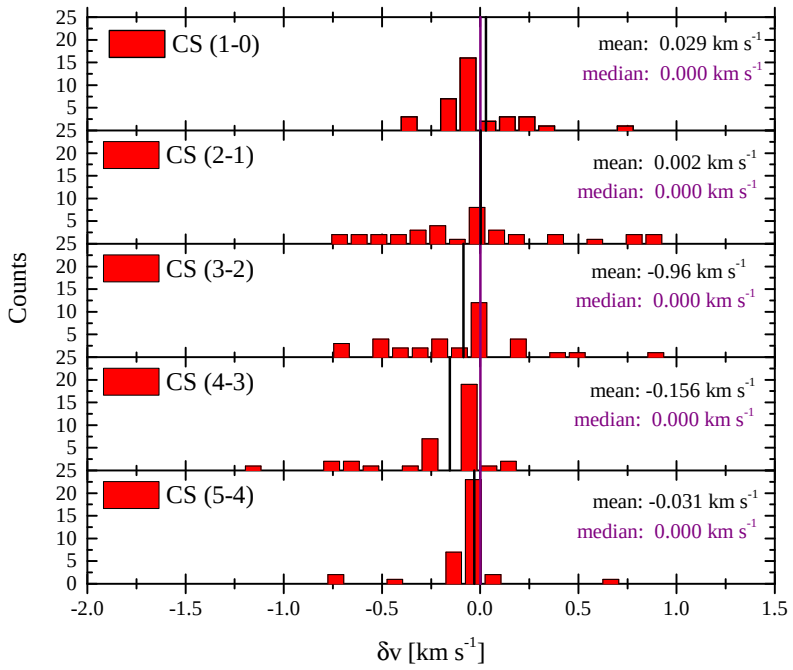

Figure A.9: Histogram of CS δv results using ^{13}CO (3-2) as reference line. As in Fig. A.1.

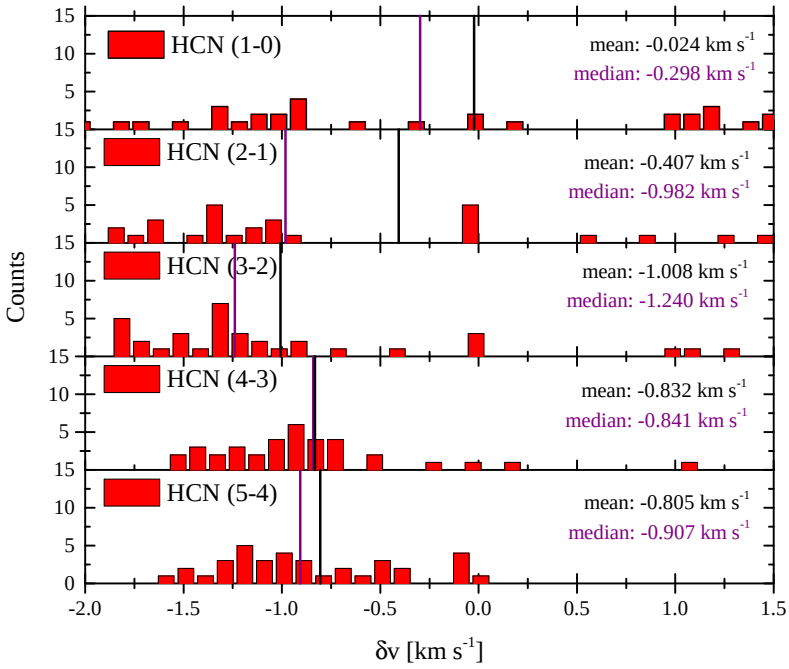

Figure A.10: Histogram of HCN δv results using $H^{13}CO^+$ (3-2) as reference line. As in Fig. A.1.

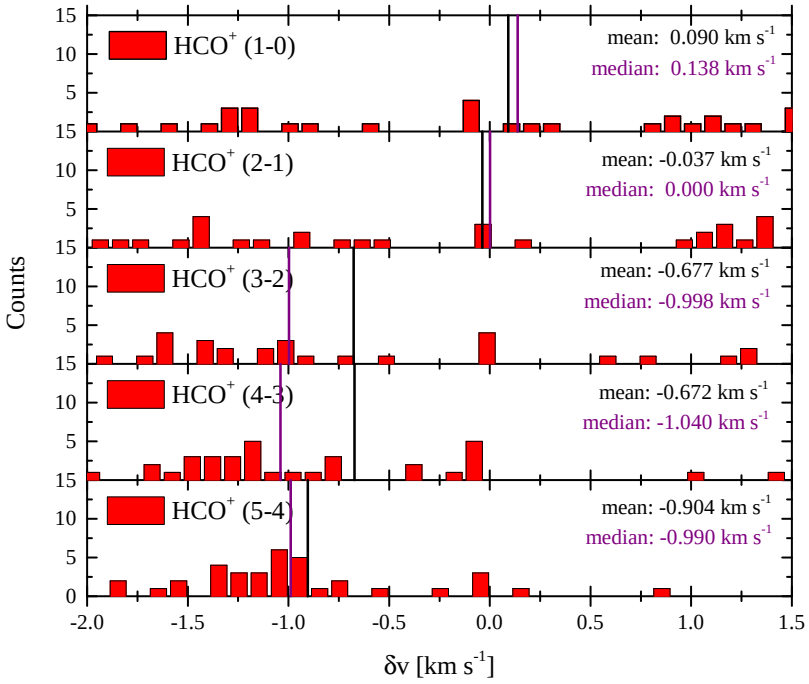

Figure A.11: Histogram of HCO^+ δv results using $H^{13}CO^+$ (3-2) as reference line. As in Fig. A.1.

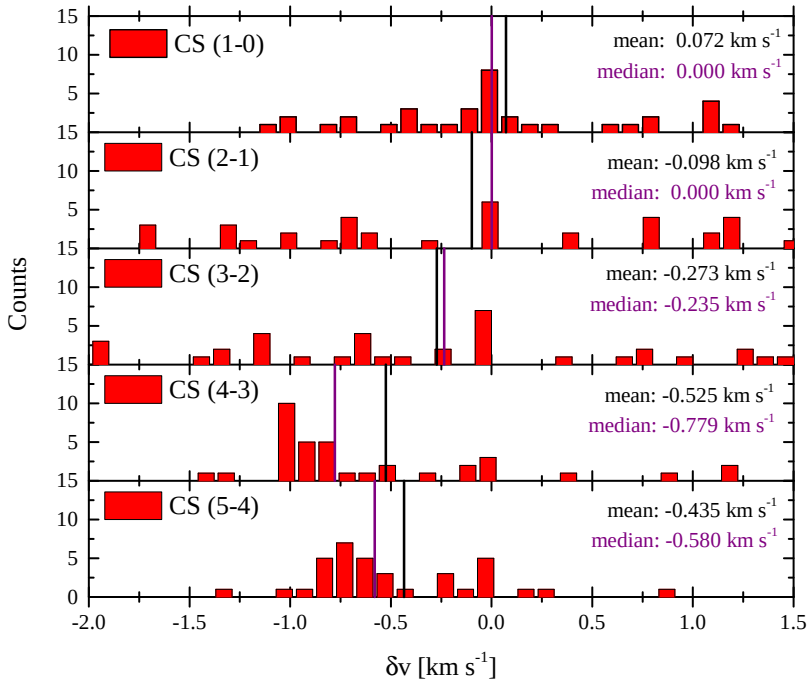

Figure A.12: Histogram of CS δv results using $H^{13}CO^+$ (3-2) as reference line. As in Fig. A.1.

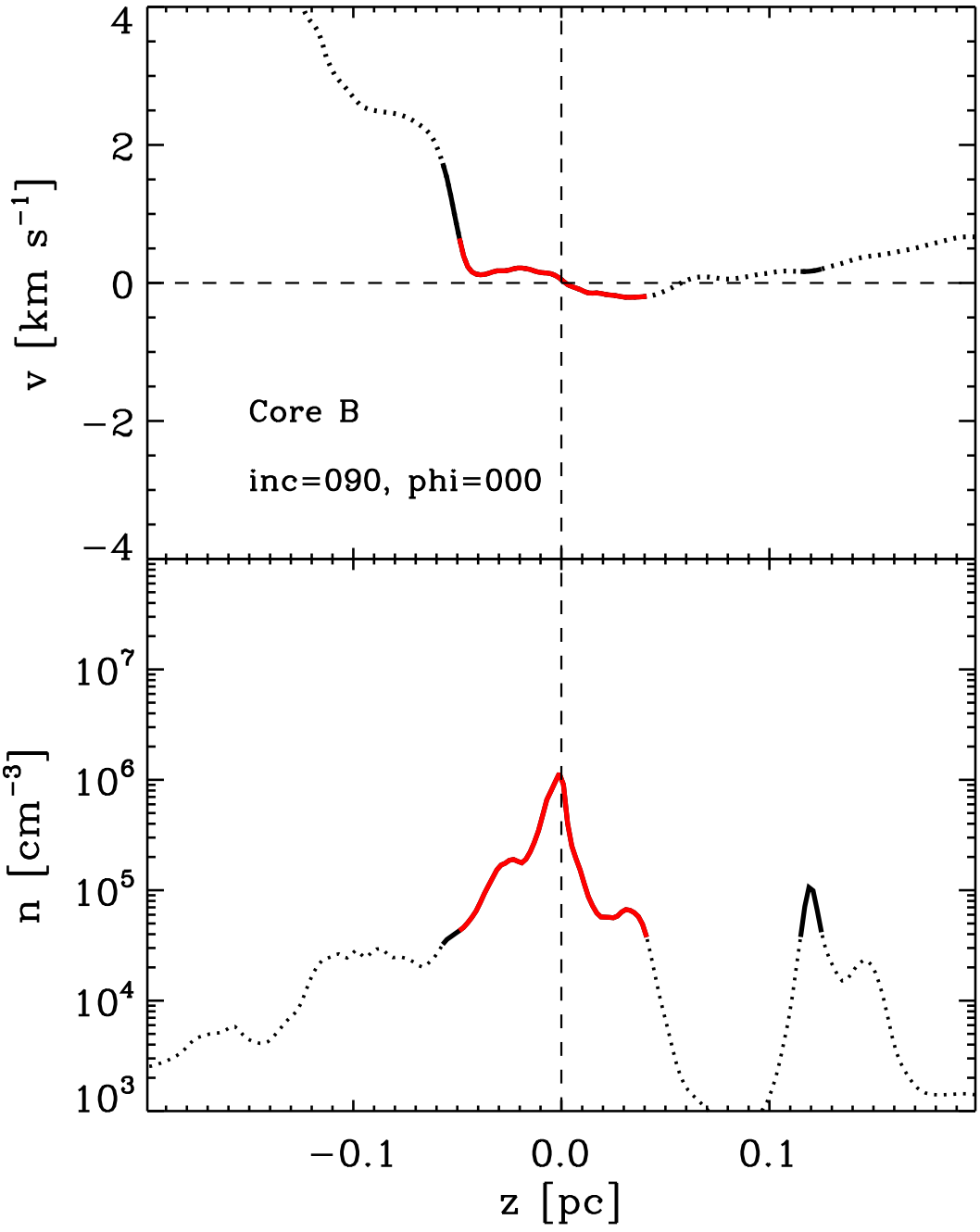

Figure A.13: $n - v$ – diagram of Core B at $i = 90°$ and $\phi = 0°$. The number density and velocity distribution are plotted with dashed lines. Thick black lines mark regions with number densities higher than 3×10^4 cm^{-3}, red lines such within a radius of 0.05 pc around the core centre.

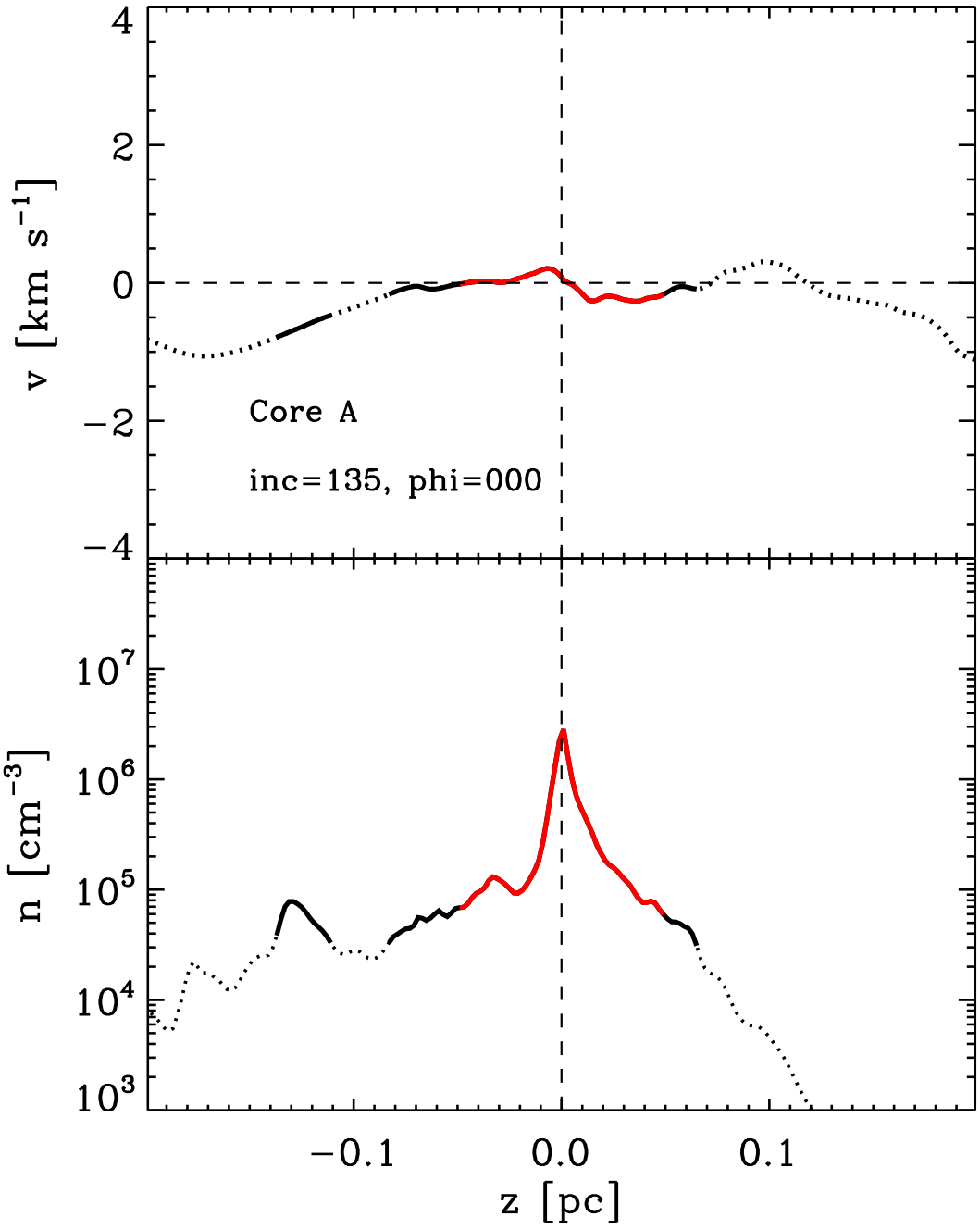

Figure A.14: $n - v$ – diagram of Core A at $i = 135°$ and $\phi = 0°$. As in Fig. A.13.

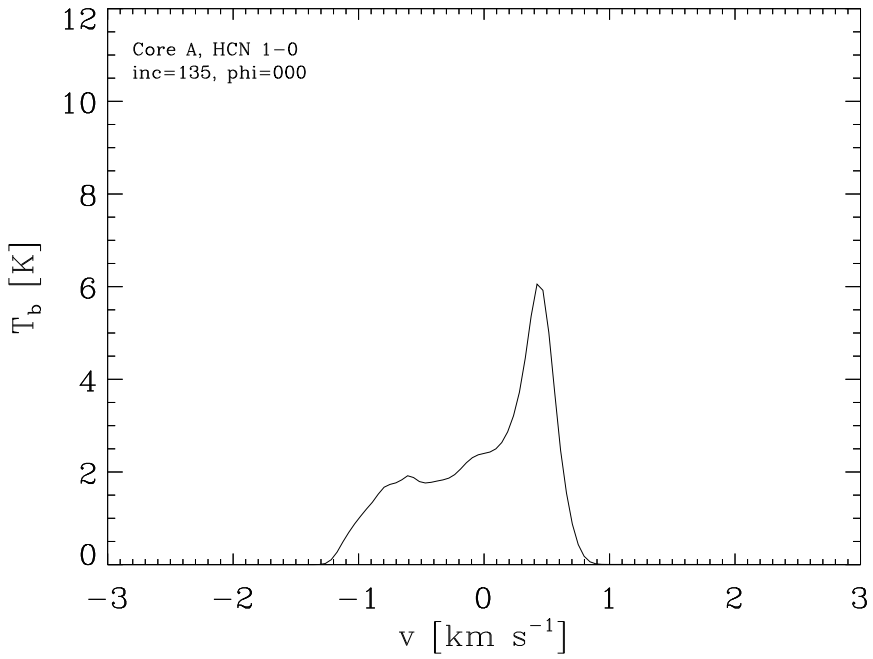

Figure A.15: Red asymmetric line profile of HCN (1-0) in Core A at $i = 135°$ and $\phi = 0°$.

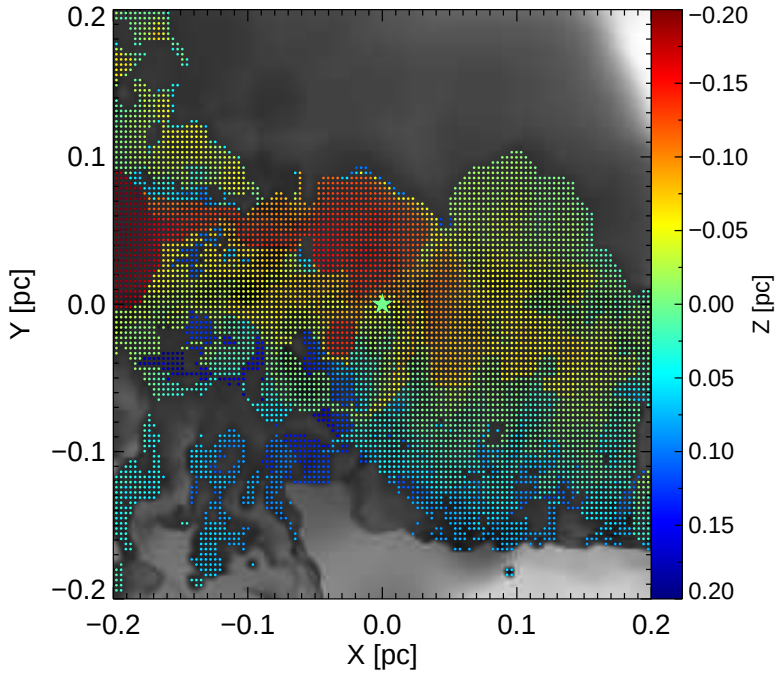

Figure A.16: Optical Depth Surface plot of HCN (1-0) in Core A at $i = 135°$ and $\phi = 0°$

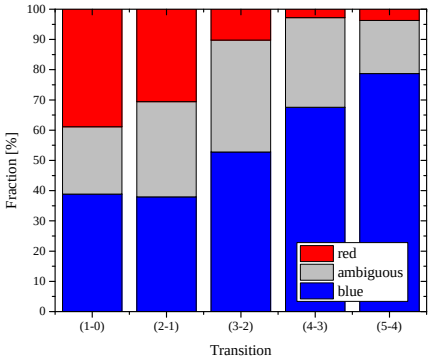

(a) N_2H^+ (1-0)

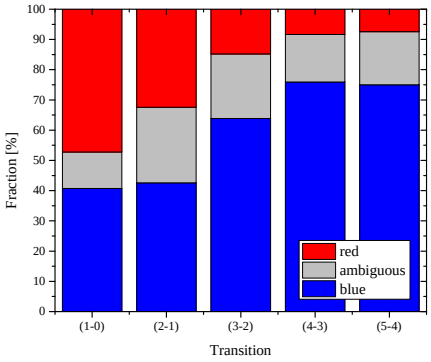

(b) N_2H^+ (3-2)

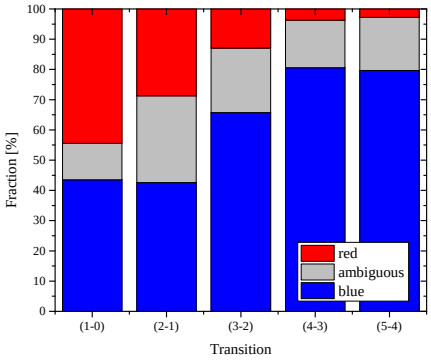

(c) $H^{13}CO^+$ (3-2)

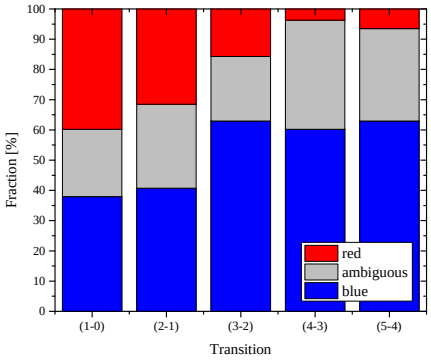

(d) ^{13}CO (3-2)

Figure A.17: Chart bars summarising the results of δv analysis using the 3σ criterion. The graphs give the fractions of blue, red asymmetric or ambiguous line profiles at each transitions for all optically thick tracers, cores and sight-lines. The total number per transition is 108. The optically thin species and transitions which have been used as references are given in the corresponding captions. With increasing transitions the numbers of blue and ambiguous line profiles increase and the ones of red profiles decrease.

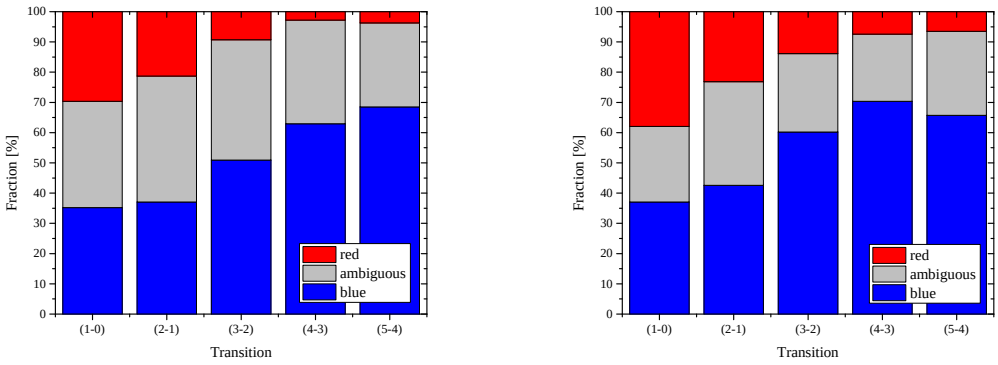

(a) N_2H^+ (1-0)

(b) N_2H^+ (3-2)

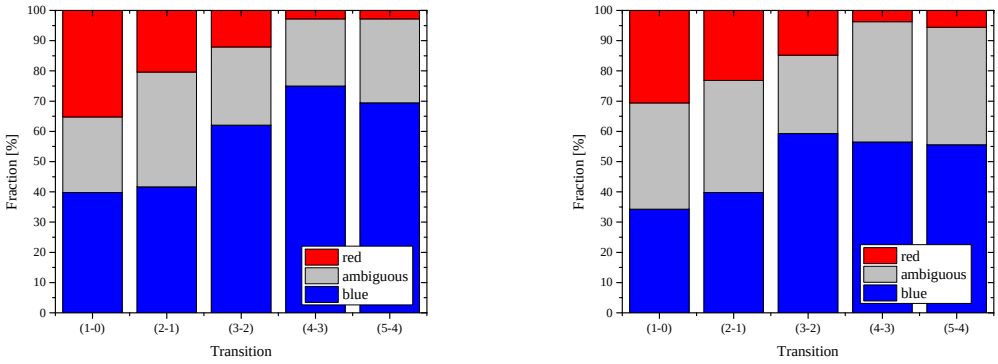

(c) $H^{13}CO^+$ (3-2)

(d) ^{13}CO (3-2)

Figure A.18: Chart bars summarising the results of δv analysis using the 5σ criterion. As in Fig. A.17.

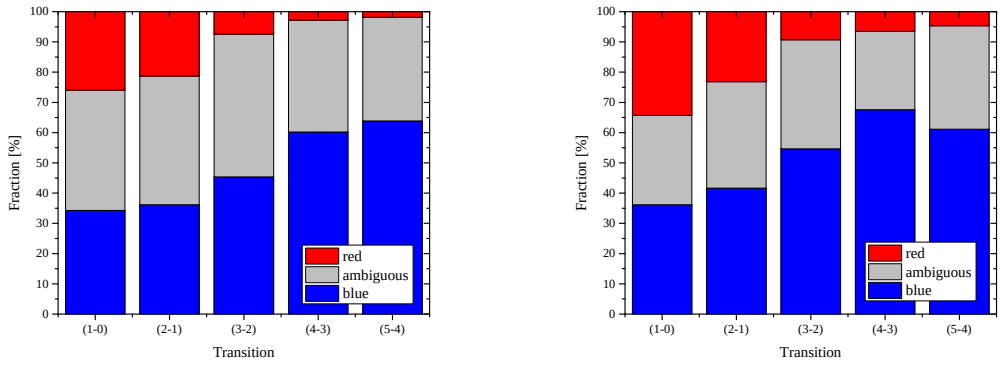

(a) N_2H^+ (1-0)

(b) N_2H^+ (3-2)

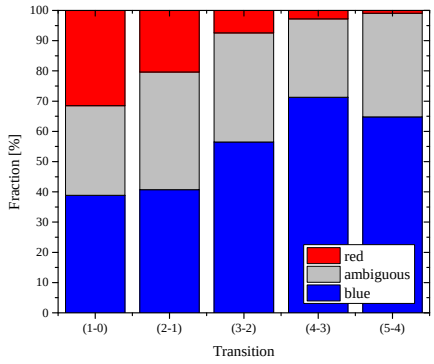

(c) $H^{13}CO^+$ (3-2)

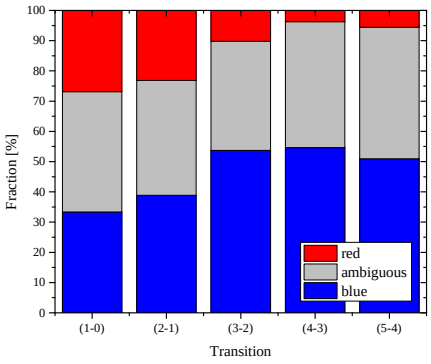

(d) ^{13}CO (3-2)

Figure A.19: Chart bars summarising the results of δv analysis using the 6σ criterion. As in Fig. A.17.

List of Figures

1.1 Carina Nebula (Credit: NASA) 1
1.2 Empirical sequence for star formation and circumstellar evolution of a single star (André 2011) 4
1.3 A 1D sketch of the potential well method for finding clumps (Smith et al. 2009a). 7
1.4 Sketch explaining the origin of blue asymmetric line profiles in collapsing, spherical cores (Smith et al. 2012). 15
1.5 Examples for line profile asymmetries. 16

2.1 Schematic illustration of `RADMC-3D` Doppler catching methods[4]. 22
2.2 n - v - diagram of Core C at i =135° and ϕ =0°. 25

3.1 (1-0) transition lines of all tracer species in all cores at $i = 0°$ and $\phi = 0°$. 28
3.2 Exemplary line profiles of HCN (1-0) and (3-2) observed in our models. . . 29
3.3 HCN (1-0) line profile and n - v - diagram of Core C at $i = 0°$ and $\phi = 0°$. 32
3.4 Chart bars of δv results 37
3.5 Example of an optical depth surface plot. 40
3.6 Line profile and optical depth surface of N_2H^+ in Core C at $i = 90°$ and $\phi = 180°$. The line profile is affected by self-absorption since N_2H^+ becomes optically thick within the observed area. 41
3.7 Line profiles and optical depth surfaces of HCN in Core B. 42
3.8 Line profiles and optical depth surfaces of N_2H^+ in Core B. 43
3.9 Histograms of results of optical depth surface analysis of HCN. 46
3.10 Histograms of results of optical depth surface analysis of HCO^+. 47
3.11 Histograms of results of optical depth surface analysis of CS. 47
3.12 Example for the influence of noise on the classification of ambiguous line profiles. 50
3.13 Chart bar summarising the results of δv analysis using a 3σ noise level as threshold. 51

3.14 Chart bar summarising the results of δv analysis using a 5σ noise level as threshold. 52
3.15 Chart bar summarising the results of δv analysis using a 6σ noise level as threshold. 52

A.1 Histogram of HCN δv results using N_2H^+ (1-0) as reference line. Going to higher transitions the distributions become narrower and the mean and median values of δv more negative. 62
A.2 Histogram of HCO^+ δv results using N_2H^+ (1-0) as reference line. As in Fig. A.1. 62
A.3 Histogram of CS δv results using N_2H^+ (1-0) as reference line. As in Fig. A.1. 63
A.4 Histogram of HCN δv results using N_2H^+ (3-2) as reference line. As in Fig. A.1. 64
A.5 Histogram of HCO^+ δv results using N_2H^+ (3-2) as reference line. As in Fig. A.1. 64
A.6 Histogram of CS δv results using N_2H^+ (3-2) as reference line. As in Fig. A.1. 65
A.7 Histogram of HCN δv results using ^{13}CO (3-2) as reference line. As in Fig. A.1. 66
A.8 Histogram of HCO^+ δv results using ^{13}CO (3-2) as reference line. As in Fig. A.1. 66
A.9 Histogram of CS δv results using ^{13}CO (3-2) as reference line. As in Fig. A.1. 67
A.10 Histogram of HCN δv results using $H^{13}CO^+$ (3-2) as reference line. As in Fig. A.1. 68
A.11 Histogram of HCO^+ δv results using $H^{13}CO^+$ (3-2) as reference line. As in Fig. A.1. 68
A.12 Histogram of CS δv results using $H^{13}CO^+$ (3-2) as reference line. As in Fig. A.1. 69
A.13 $n - v$ – diagram of Core B at $i = 90°$ and $\phi = 0°$ 70
A.14 $n - v$ – diagram of Core A at $i = 135°$ and $\phi = 0°$. As in Fig. A.13. . . . 71
A.15 Red asymmetric line profile of HCN (1-0) in Core A at $i = 135°$ and $\phi = 0°$. 72
A.16 Optical Depth Surface plot of HCN (1-0) in Core A at $i = 135°$ and $\phi = 0°$ 72
A.17 Chart bars of δv results with 3σ criterion. 73
A.18 Chart bars of δv results with 5σ criterion. 74

A.19 Chart bars of δv results with 6σ criterion. 75

List of Tables

1.1 Properties of clouds, cores and cores (adapted from Bergin & Tafalla 2007). 6
1.2 Properties of tracers. An overview. 19

2.1 Abundances of Molecular Tracers. 22

3.1 Summary of δv analysis using N_2H^+ (1-0) as a reference line. 35
3.2 Summary of δv analysis using N_2H^+ (3-2) as a reference line. 35
3.3 Summary of δv analysis using $H^{13}CO^+$ (3-2) as a reference line. 36
3.4 Summary of δv analysis using ^{13}CO (3-2) as a reference line. 36
3.5 Summary of measured brightness temperatures. 48

A.1 Detailed list of frequences, wavelengths and critical densities for each tracer and transition. 60

Bibliography

Aguirre, J. E., Ginsburg, A. G., Dunham, M. K., et al. 2011, Astrophys. J. Suppl., 192, 4

Aikawa, Y., Herbst, E., Roberts, H., & Caselli, P. 2005, Astrophys. J. , 620, 330

Alves, J., Lombardi, M., & Lada, C. 2007, The Origin of the Initial Mass Function is in the Cloud Structure, ed. R. S. de Jong, 417

André, P., Belloche, A., Motte, F., & Peretto, N. 2007, Astron. Astrophys. , 472, 519

André, P., Men'shchikov, A., Bontemps, S., et al. 2010, Astron. Astrophys. , 518, L102

Andre, P., Ward-Thompson, D., & Barsony, M. 1993, Astrophys. J. , 406, 122

André, P. 2011, Spectral Classification of Embedded Stars, ed. M. Gargaud, R. Amils, J. Quintanilla, I. Cleaves, HendersonJames (Jim), W. Irvine, D. Pinti, & M. Viso (Springer Berlin Heidelberg), 1549–1553

Arzoumanian, D., André, P., Didelon, P., et al. 2011, Astron. Astrophys. , 529, L6

Bate, M. R. & Burkert, A. 1997, Monthly Notices Roy. Astron. Soc. , 288, 1060

Bergin, E. A., Alves, J., Huard, T., & Lada, C. J. 2002, Astrophys. J. Letters, 570, L101

Bergin, E. A. & Tafalla, M. 2007, Ann. Rev. Astron. Astrophys. , 45, 339

Böhm-Vitense, E. 1989, Introduction to stellar astrophysics. Vol. 2. Stellar atmospheres.

Bonnell, I. A., Bate, M. R., Clarke, C. J., & Pringle, J. E. 1997, Monthly Notices Roy. Astron. Soc. , 285, 201

Bonnell, I. A., Bate, M. R., Clarke, C. J., & Pringle, J. E. 2001, Monthly Notices Roy. Astron. Soc. , 323, 785

Bonnell, I. A., Bate, M. R., & Zinnecker, H. 1998, Monthly Notices Roy. Astron. Soc. , 298, 93

Buhl, D. & Snyder, L. E. 1970, Nature, 228, 267

Carolan, P. B., Redman, M. P., Keto, E., & Rawlings, J. M. C. 2008, Monthly Notices Roy. Astron. Soc. , 383, 705

Caselli, P., Walmsley, C. M., Zucconi, A., et al. 2002, Astrophys. J. , 565, 331

Chabrier, G. 2002, Astrophys. J. , 567, 304

Dale, J. E. & Bonnell, I. A. 2008, Monthly Notices Roy. Astron. Soc. , 391, 2

Daniel, F., Dubernet, M.-L., Meuwly, M., Cernicharo, J., & Pagani, L. 2005, Monthly Notices Roy. Astron. Soc. , 363, 1083

Dumouchel, F., Faure, A., & Lique, F. 2010, Monthly Notices Roy. Astron. Soc. , 406, 2488

Egan, M. P., Shipman, R. F., Price, S. D., et al. 1998, Astrophys. J. , 494, L199+

Elmegreen, B. G. 1993, in Protostars and Planets III, ed. E. H. Levy & J. I. Lunine, 97–124

Elmegreen, B. G., Efremov, Y., Pudritz, R. E., & Zinnecker, H. 2000, Protostars and Planets IV, 179

Elmegreen, B. G. & Mathieu, R. D. 1983, Monthly Notices Roy. Astron. Soc. , 203, 305

Evans, II, N. J. 1999, Ann. Rev. Astron. Astrophys. , 37, 311

Flower, D. R. 1999, Monthly Notices Roy. Astron. Soc. , 305, 651

Fuller, G. A., Williams, S. J., & Sridharan, T. K. 2005, Astron. Astrophys. , 442, 949

Goodwin, S. P., Nutter, D., Kroupa, P., Ward-Thompson, D., & Whitworth, A. P. 2008, Astron. Astrophys. , 477, 823

Green, S. & Thaddeus, P. 1974, Astrophys. J. , 191, 653

Gregersen, E. M. & Evans, II, N. J. 2000, Astrophys. J. , 538, 260

Gregersen, E. M., Evans, II, N. J., Zhou, S., & Choi, M. 1997, Astrophys. J. , 484, 256

Hacar, A. & Tafalla, M. 2011, Astron. Astrophys. , 533, A34

Hartmann, L. & Burkert, A. 2007, Astrophys. J. , 654, 988

Heitsch, F., Mac Low, M.-M., & Klessen, R. S. 2001, Astrophys. J. , 547, 280

Inutsuka, S.-I. & Miyama, S. M. 1997, Astrophys. J. , 480, 681

Jeans, J. H. 1902, Royal Society of London Philosophical Transactions Series A, 199, 1

Klessen, R. S., Heitsch, F., & Mac Low, M.-M. 2000, Astrophys. J. , 535, 887

Kroupa, P. 2002, Science, 295, 82

Lada, C. J. 1987, in IAU Symposium, Vol. 115, Star Forming Regions, ed. M. Peimbert & J. Jugaku, 1–17

Lada, C. J. & Lada, E. A. 2003, Ann. Rev. Astron. Astrophys. , 41, 57

Larson, R. B. 1973, Monthly Notices Roy. Astron. Soc. , 161, 133

Larson, R. B. 2003, Reports on Progress in Physics, 66, 1651

Lee, C. W. & Myers, P. C. 2011, Astrophys. J. , 734, 60

Lee, C. W., Myers, P. C., & Tafalla, M. 1999, Astrophys. J. , 526, 788

Lee, J.-E., Bergin, E. A., & Evans, II, N. J. 2004, Astrophys. J. , 617, 360

Mac Low, M.-M. 2003, in Lecture Notes in Physics, Berlin Springer Verlag, Vol. 614, Turbulence and Magnetic Fields in Astrophysics, ed. E. Falgarone & T. Passot, 182–212

Mac Low, M.-M. & Klessen, R. S. 2004, Reviews of Modern Physics, 76, 125

Mardones, D., Myers, P. C., Tafalla, M., et al. 1997, Astrophys. J. , 489, 719

Maruta, H., Nakamura, F., Nishi, R., Ikeda, N., & Kitamura, Y. 2010, Astrophys. J. , 714, 680

McKee, C. F. & Tan, J. C. 2003, Astrophys. J. , 585, 850

Monaghan, J. J. 1992, Ann. Rev. Astron. Astrophys. , 30, 543

Motte, F., Andre, P., & Neri, R. 1998, Astron. Astrophys. , 336, 150

Myers, P. C. 2008, Astrophys. J. , 687, 340

Myers, P. C., Adams, F. C., Chen, H., & Schaff, E. 1998, Astrophys. J. , 492, 703

Myers, P. C., Mardones, D., Tafalla, M., Williams, J. P., & Wilner, D. J. 1996, Astrophys. J. Letters, 465, L133

Ostriker, E. C., Gammie, C. F., & Stone, J. M. 1999, Astrophys. J. , 513, 259

Ostriker, E. C., Stone, J. M., & Gammie, C. F. 2001, Astrophys. J. , 546, 980

Padoan, P., Juvela, M., Goodman, A. A., & Nordlund, Å. 2001, Astrophys. J. , 553, 227

Padoan, P. & Nordlund, Å. 2002, Astrophys. J. , 576, 870

Perault, M., Omont, A., Simon, G., et al. 1996, Astron. Astrophys. , 315, L165

Peretto, N., André, P., & Belloche, A. 2006, Astron. Astrophys. , 445, 979

Peretto, N., André, P., Könyves, V., et al. 2012, Astron. Astrophys. , 541, A63

Peretto, N. & Fuller, G. A. 2009, Astron. Astrophys. , 505, 405

Pilbratt, G. L., Riedinger, J. R., Passvogel, T., et al. 2010, Astron. Astrophys. , 518

Pineda, J. E., Caselli, P., & Goodman, A. A. 2008, Astrophys. J. , 679, 481

Pontoppidan, K. M., Meijerink, R., Dullemond, C. P., & Blake, G. A. 2009, Astrophys. J. , 704, 1482

Rawlings, J. M. C. & Yates, J. A. 2001, Monthly Notices Roy. Astron. Soc. , 326, 1423

Schenck, D. E., Shirley, Y. L., Reiter, M., & Juneau, S. 2011, Astron. J., 142, 94

Schöier, F. L., van der Tak, F. F. S., van Dishoeck, E. F., & Black, J. H. 2005, A&A, 432, 369

Schuller, F., Menten, K. M., Contreras, Y., et al. 2009, Astron. Astrophys. , 504, 415

Shetty, R., Glover, S. C., Dullemond, C. P., & Klessen, R. S. 2011, Monthly Notices Roy. Astron. Soc. , 412, 1686

Shu, F. H., Lizano, S., Ruden, S. P., & Najita, J. 1988, Astrophys. J. Letters, 328, L19

Silk, J. 1995, Astrophys. J. Letters, 438, L41

Simon, R., Jackson, J. M., Rathborne, J. M., & Chambers, E. T. 2006, Astrophys. J. , 639, 227

Smith, R. J., Clark, P. C., & Bonnell, I. A. 2009a, Monthly Notices Roy. Astron. Soc. , 396, 830

Smith, R. J., Glover, S. C. O., Bonnell, I. A., Clark, P. C., & Klessen, R. S. 2011, Monthly Notices Roy. Astron. Soc. , 411, 1354

Smith, R. J., Longmore, S., & Bonnell, I. 2009b, Monthly Notices Roy. Astron. Soc. , 400, 1775

Smith, R. J., Shetty, R., Stutz, A. M., & Klessen, R. S. 2012, Astrophys. J. , 750, 64

Snyder, L. E. & Buhl, D. 1971, Astrophys. J. Letters, 163, L47

Sobolev, V. V. 1957, Soviet Astronomy, 1, 678

Sohn, J., Lee, C. W., Park, Y.-S., et al. 2007, Astrophys. J. , 664, 928

Stahler, S. W. & Yen, J. J. 2010, Monthly Notices Roy. Astron. Soc. , 407, 2434

Tafalla, M., Myers, P. C., Caselli, P., & Walmsley, C. M. 2004, Astron. Astrophys. , 416, 191

Tafalla, M., Myers, P. C., Caselli, P., Walmsley, C. M., & Comito, C. 2002, Astrophys. J. , 569, 815

Tennyson, J. 2005, Astronomical spectroscopy : an introduction to the atomic and molecular physics of astronomical spectra

Tilley, D. A. & Pudritz, R. E. 2007, Monthly Notices Roy. Astron. Soc. , 382, 73

Tohline, J. E. 1982, Fundamentals of Cosmic Physics, 8, 1

Tsamis, Y. G., Rawlings, J. M. C., Yates, J. A., & Viti, S. 2008, Monthly Notices Roy. Astron. Soc. , 388, 898

Turner, B. E. 1974, Astrophys. J. Letters, 193, L83

Turner, B. E., Chan, K.-W., Green, S., & Lubowich, D. A. 1992, Astrophys. J. , 399, 114

Walker, C. K., Narayanan, G., & Boss, A. P. 1994, Astrophys. J. , 431, 767

Werner, M. W., Roellig, T. L., Low, F. J., et al. 2004, Astrophys. J. , 154, 1

Williams, J. P., Blitz, L., & McKee, C. F. 2000, Protostars and Planets IV, 97

Wu, J. & Evans, II, N. J. 2003, Astrophys. J. Letters, 592, L79

Wu, Y., Liu, T., Meng, F., et al. 2012, Astrophys. J. , 756, 76

Yang, B., Stancil, P. C., Balakrishnan, N., & Forrey, R. C. 2010, Astrophys. J. , 718, 1062

Zhou, S. 1992, Astrophys. J. , 394, 204

Zhou, S., Evans, II, N. J., Guesten, R., Mundy, L. G., & Kutner, M. L. 1991, Astrophys. J. , 372, 518

Zhou, S., Evans, II, N. J., Koempe, C., & Walmsley, C. M. 1993, Astrophys. J. , 404, 232

Zinnecker, H. 1982, Annals of the New York Academy of Sciences, 395, 226

Acknowledgements

I want to thank many people. Without their help I would not have come so far.
First of all I thank Prof. Dr. Ralf Klessen who offered me to work in his star formation group at the Institute for Theoretical Astrophysics and gain a deeper insight in the theoretical considerations of star-formation. I enjoyed working and discussing with him, my supervisor Dr. Rowan Smith and the the rest of the group. Especially thanks to Rowan's patience while correcting this thesis.
Thanks also to Prof. Dr. Cornelis Dullemond who has supported me with his help, taught me a lot about radiative transfer and agreed to be the second corrector of this thesis.
Furthermore, I want to thank my Masters colleagues, Adriana, Clio, Carsten, Tilmann and Sebastian, for creating a great atmosphere in the office.
Finally, special thanks go to my friends, especially my best friend Karina, and family for their support. Without them, I would not have come that far.

Erklärung / Affidavit

Ich versichere hiermit, dass ich diese Masterarbeit selbständig verfasst und nur die angegebenen Quellen und Hilfsmittel verwendet habe.

With this, I assure that I have authored this Master thesis by my own and used only the named sources and aids.

Heidelberg, August 14, 2013

.....

(Unterschrift des Kandidaten)